



HAL
open science

Relations between the characteristics of granular column collapses and resultant high-frequency seismic signals

Maxime Farin, Anne Mangeney, Julien de Rosny, Renaud Toussaint,
Phuong-Thu Trinh

► To cite this version:

Maxime Farin, Anne Mangeney, Julien de Rosny, Renaud Toussaint, Phuong-Thu Trinh. Relations between the characteristics of granular column collapses and resultant high-frequency seismic signals. *Journal of Geophysical Research: Earth Surface*, 2019, 10.1029/2019JF005258 . insu-02333954

HAL Id: insu-02333954

<https://insu.hal.science/insu-02333954>

Submitted on 31 Oct 2019

HAL is a multi-disciplinary open access archive for the deposit and dissemination of scientific research documents, whether they are published or not. The documents may come from teaching and research institutions in France or abroad, or from public or private research centers.

L'archive ouverte pluridisciplinaire **HAL**, est destinée au dépôt et à la diffusion de documents scientifiques de niveau recherche, publiés ou non, émanant des établissements d'enseignement et de recherche français ou étrangers, des laboratoires publics ou privés.

1 **Relations Between the Characteristics of Granular**
2 **Column Collapses and that of the Generated**
3 **High-frequency Seismic Signal**

4 **Maxime Farin^{1,2*}, Anne Mangeney^{2,3}, Julien de Rosny¹, Renaud Toussaint^{4,5},**
5 **and Phuong-Thu Trinh⁶**

6 .

7 ¹Institut Langevin, ESPCI Paris, PSL Research University, CNRS, Paris, France

8 ²Institut de Physique du Globe de Paris, Sorbonne Paris Cité, CNRS (UMR 7154), Paris, France

9 ³ANGE team, CEREMA, Inria, Lab. J.-L. Lions, CNRS, Paris, France

10 ⁴Institut de Physique du Globe de Strasbourg/EOST, CNRS, Strasbourg, France

11 ⁵ SFF PoreLab, The Njord Centre, Department of Physics, University of Oslo, Oslo, Norway

12 ⁶Total SA, Pau, France

13 **Key Points:**

- 14 • = We conduct granular column collapse experiments with various initial condi-
15 tions and seismic measurements.
- 16 • = Empirical scaling laws are established between the dynamics and seismic pa-
17 rameters.
- 18 • = The increase of radiated seismic energy with slope angle matches with the in-
19 crease in particle agitation.

*Institut Langevin, ESPCI Paris, PSL Research University, CNRS, 1 rue Jussieu, Paris, France

Corresponding author: Maxime Farin, maxime.farin@espci.fr

Abstract

Deducing relations between the dynamic characteristics of landslides and rockfalls and the generated high-frequency (> 1 Hz) seismic signal is challenging. In order to get some insights into what relations could be tested in the field, we conduct laboratory experiments of granular column collapse on a rough inclined thin plate, for a large set of column masses, aspect ratios, particle diameters and slope angles. The dynamics of the granular flows is recorded using a high speed camera and the generated seismic signal is measured using piezoelectric accelerometers. Empirical scaling laws are established between the characteristics of the granular flows and deposits and that of the generated seismic signals. The radiated seismic energy scales with particle diameter as d^3 , column mass as M , aspect ratio as $a^{1.1}$ and initial column height as H_0^2 . The increase of the radiated seismic energy as slope angle increases correlates with a similar increase in particle agitation. We interpret that the discrepancy of our empirical scaling laws with relations reported in the field can be explained by the complex influence of the substrate on seismic signal and the difference of flow initiation in both cases. However, our empirical scaling laws allow us to determine which flow parameters could be inferred from a given seismic characteristic in the field. In particular, by assuming the flow average speed is known, we show that we can retrieve parameters d , a and M within a factor of two from the seismic signal.

1 Introduction

Over the last two decades, seismic signals generated by granular flows (e.g. landslides, debris flows and rockfalls) have been more and more investigated, as a useful complementary tool to sparse visual observations, in order to detect flows and deduce informations about their localization and dynamics [e.g., *Arattano, 2000; Brodsky et al., 2003; Suriñach et al., 2005; Huang et al., 2007; Dammeier et al., 2011; Hibert et al., 2014a, 2017a,b; Kean et al., 2015; Zhao et al., 2015; Pérez-Guillén et al., 2016; Yamada et al., 2016; Lai et al., 2018*].

The high-frequency content (> 1 Hz) of the seismic signal is likely mostly generated by the numerous impacts of the particles composing the granular flows [*Huang et al., 2007; Hsu et al., 2014; Hibert et al., 2017c; Farin et al., 2018, 2019*]. An important parameter that may control high-frequency seismic amplitude is the fluctuating speed of

51 the particles, that is a measurement of the state of agitation of particles [often referred
52 to as ‘granular temperature’, e.g. *Andreotti et al.*, 2013; *Delannay et al.*, 2017]. Fluctu-
53 ating speed of the particle controls the rate of particle impacts [*Andreotti et al.*, 2013]
54 and most probably the impact forces imparted by particles at the bed of granular flows
55 [*Farin et al.*, 2019]. Therefore, the high-frequency signal is suspected to contain quan-
56 titative informations about characteristics of a granular flow and of the particles com-
57 posing it, such as the size of the particles, the flowing volume (i.e. number of particles
58 available to impact the bed) and the flow momentum (i.e. speed of the particles).

59 Only a few field studies could establish analytical scaling laws relating the flow pa-
60 rameters to the characteristics of the high-frequency seismic signal. The generally ob-
61 served trend is that the maximum seismic amplitude A_{max} and absolute seismic energy
62 W_{el} of the radiated seismic signal increases with the flow volume V , or particle mass/diameter
63 in the case of individual block release [*Norris*, 1994; *Dammeier et al.*, 2011; *Hibert et al.*,
64 2011, 2017c; *Yamada et al.*, 2012; *Farin et al.*, 2015]. However, the reported empirical
65 scaling laws relating these parameters seem to slightly depend on the investigated land-
66 slide site. For example, *Norris* [1994] and *Yamada et al.* [2012] noted that the maximum
67 seismic amplitude A_{max} is proportional to the flow volume V for large landslides, while
68 *Hibert et al.* [2011] rather reported a proportionality between the seismic energy W_{el} (\propto
69 A_{max}^2) generated by rockfalls and their volume V for small rockfalls that occurred in the
70 Dolomieu crater of the Piton de la Fournaise volcano, Reunion Island. In contrast, a more
71 complex empirical relationship $V \propto t_s^{1.0368} EA^{-0.1248} A_{max}^{1.1446}$ with t_s , the flow duration
72 and EA , the seismic envelope area, was found by *Dammeier et al.* [2011] using a statis-
73 tical approach for 20 rockfall events. *Hibert et al.* [2017a] observed a good temporal cor-
74 relation between the modulus of the momentum of the flow and the amplitude of the smoothed
75 envelope of the seismic signal in the frequency range 3 to 10 Hz, for twelve worldwide
76 large landslides. Moreover, they showed that the maximum seismic amplitude is propor-
77 tional to the flow momentum. In the case of individual rock blocks impacts on a steep
78 slope, the best fit to the seismic data shows a dependence of the radiated seismic energy
79 W_{el} to the particle mass m and impact speed v_z as $mv_z^{0.5}$ [*Farin et al.*, 2015] or $mv_z^{13/5}$
80 [*Hibert et al.*, 2017c], based on analytical scaling laws for a sphere impacting a thick block
81 established by *Farin et al.* [2015].

82 Most studies on the high-frequency seismic signal generated by granular flows were
83 only able to observe a relative change in the seismic signal amplitude with a relative vari-

84 ation of a flow characteristic, if the other flow characteristics remain approximately con-
 85 stant [e.g. *Arattano, 2000; Huang et al., 2007; Suriñach et al., 2005; Burtin et al., 2009;*
 86 *Kean et al., 2015*]. For example, *Huang et al. [2007]* noted that the frequency of the seis-
 87 mic signal generated by debris flows decreases when the diameter of the involved par-
 88 ticles increases. By comparing the seismic power generated by successive debris flows in
 89 the same channel, *Kean et al. [2015]* related the increase of seismic power between two
 90 debris flows to the decrease of the thickness of the underlying erodible sediment bed. Es-
 91 tablishing clear quantitative scaling relations between the generated high-frequency seis-
 92 mic signal and flow parameters is difficult in the field because of numerous yet unparsed
 93 complexities. First, flows are heterogeneous, partly due to particle segregation [*Iverson,*
 94 *1997; Kean et al., 2015*], make it challenging to deduce one flow parameter (flow thick-
 95 ness, speed or particle diameter) from one seismic measurement. Then, irregularities in
 96 the bed topography such as turns and bumps and the presence of an erodible bed can
 97 cause a sudden increase or decrease in seismic amplitude along the flow path [*Favreau*
 98 *et al., 2010; Allstadt, 2013; Moretti et al., 2015; Kean et al., 2015; Bachelet et al., 2018a*].
 99 In addition to the flow parameters, complex path effects (e.g. attenuation, dispersion of
 100 seismic wave), due to the heterogeneity of the ground, have a strong impact on the am-
 101 plitude of the observed seismic signal [*Aki and Richards, 1980*]. Finally, visual observa-
 102 tions of the dynamics of gravitational instabilities are rare due to the dangerousness and
 103 unpredictability of these events, which makes it harder to interpret the observed seis-
 104 mic amplitudes.

105 Most of these complexities are not present in acoustically monitored laboratory ex-
 106 periments of granular flows. Such experiments offer a convenient way to investigate the
 107 individual effect of each flow parameter on the generated seismic signal by varying one
 108 parameter while fixing the others. The dynamics of granular flows and the effect of the
 109 parameters of a released granular column on its runout distance has been extensively in-
 110 vestigated in the laboratory during the past few decades [see e.g. *GdR Midi, 2004; An-*
 111 *dreotti et al., 2013; Delannay et al., 2017*, for review]. In particular, authors reported that
 112 the runout distance r_f of granular flow is proportional to the initial height H_0 of the re-
 113 leased granular column, regardless of the other flow parameters (volume, initial aspect
 114 ratio (i.e. height over length of the column) and particle shape, diameter and material)
 115 [e.g. *Balmforth and Kerswell, 2005; Lube et al., 2005; Siavoshi and Kudrolli, 2005; Hogg,*
 116 *2007; Mangeney et al., 2010; Lube et al., 2011; Farin et al., 2014*]. While r_f can be uniquely

117 determined by H_0 for horizontal flows, *Mangeney et al.* [2010] showed analytically that
 118 r_f also increases with slope angle θ as

$$119 \quad r_f \propto \frac{H_0}{\tan \delta - \tan \theta}, \quad (1)$$

120 where δ is the friction angle of the granular material. This scaling law has been validated
 121 for granular flows with a variety of volumes and aspect ratios (i.e. initial height over length
 122 of the granular column) for moderate slope angles $\theta < 15^\circ$ [*Farin et al.*, 2014]. How-
 123 ever, for higher slope angles $\theta > 15^\circ$, the scaling law does not match the data as well
 124 [*Farin et al.*, 2014]. The origin of this discrepancy is thought to be related to a transi-
 125 tion of the granular flow dynamics towards a regime with a long duration phase of slow
 126 flow velocity at the end of granular flow propagation at high slope angles θ , which ex-
 127 tends significantly the runout distance of granular flows compared to more moderate slopes
 128 ($< 10^\circ$) [*Mangeney et al.*, 2010; *Farin et al.*, 2014].

129 Recently, a few studies have investigated the boundary forces or seismic signal gen-
 130 erated by particle impacts and granular flows using vibration sensors [e.g. *Huang et al.*,
 131 2004; *Yohannes et al.*, 2012; *Hsu et al.*, 2014; *Barrière et al.*, 2015; *Farin et al.*, 2015;
 132 *Turkaya et al.*, 2015; *Taylor and Brodsky*, 2017; *Farin et al.*, 2018; *Bachelet et al.*, 2018a;
 133 *Turquet et al.*, 2018, 2019]. For example, *Yohannes et al.* [2012] and *Hsu et al.* [2014] mea-
 134 sured the distribution of fluctuating forces at the base of dry and saturated granular flows
 135 in a rotating drum using force sensors. *Farin et al.* [2015] established analytical scaling
 136 laws relating the seismic energy radiated by particle impacts and the average frequency
 137 of the generated seismic signal to the particle mass and impact speed and validated these
 138 laws with laboratory experiments of impacts of particles of various diameters and ma-
 139 terials. In particular, it was noted that the scaling laws have different coefficients when
 140 the impacts occur on thin plates or on thick blocks. The coefficients of these laws were
 141 also shown to vary when the impacts occur on a rough bed or on erodible beds of var-
 142 ious thicknesses [*Bachelet et al.*, 2018a]. *Barrière et al.* [2015] measured the acoustic sig-
 143 nal generated at the base of granular flows in a flume with a hydrophone attached un-
 144 der the flume and established an empirical scaling law relating the 50th percentile par-
 145 ticle diameter D_{50} of the particle distribution in the granular flows to the maximum am-
 146 plitude A_{max} and average frequency f_{mean} of the generated acoustic signal: $D_{50} \approx 5.0 \cdot$
 147 $10^4 A_{max}^{0.39} / f_{mean}^{0.86}$. *Turkaya et al.* [2015] and *Turquet et al.* [2018, 2019] characterized the
 148 acoustic emissions of confined granular material in Hele-Shaw cells during shear and com-
 149 paction caused by internal gas flow. Finally, *Taylor and Brodsky* [2017] conducted gran-

150 ular shearing experiments under constant confining pressure in a torsional rheometer on
151 which a piezoelectric accelerometer was attached. They asserted that the acoustic en-
152 ergy radiated by the shearing was a proxy for the granular temperature and observed
153 a linear relation between this acoustic energy and the inertial number, that quantifies
154 the relative importance of inertia and confining stresses in the granular flow [*GdR Midi*,
155 2004]. Moreover, they showed that the ratio of acoustic energy over inertial number in-
156 creases as the cube of the particle diameter.

157 In a previous paper, we performed seismically monitored 3D granular column col-
158 lapse experiments on a rough inclined thin plate, with slope angle varying from the hor-
159 izontal to 20° [*Farin et al.*, 2018]. The seismic signal generated by the granular flows was
160 measured using piezoelectric accelerometers and the dynamics of the granular flows was
161 recorded with a fast camera, allowing us to directly compare the seismic and dynamic
162 properties of these flows. The main observations of this study were

- 163 1. The shapes of the temporal variation of the normalized radiated seismic energy
164 and of the normalized potential energy lost by the granular flow match.
- 165 2. The shape of the seismic envelope changes when slope angle increases. We attributed
166 this change of shape to the development of a different dynamic regime of the gran-
167 ular flows at high slope angles, from a dense flow to a more agitated and dilute
168 flow. In both of these granular regimes, the motion of particles is ruled by colli-
169 sions between themselves and with the bed [inertial flows, see *Andreotti et al.*, 2013].
170 Within the dense flow, the rate of particle impacts is high but particle have low
171 relative speeds. In contrast, in the dilute regime, observed at the flow front with
172 a cloud of particles rebounding high above the bed (saltating front), the rate of
173 particle impacts is lower but particles impart stronger forces on the bed, poten-
174 tially generating higher seismic energy than in the flow rear.
- 175 3. The amplitude of the seismic envelope seems more related with the speed of the
176 flow center-of-mass in the direction normal to the plate during the rise phase (ac-
177 celeration phase of the flow). In contrast, the maximum seismic amplitude matches
178 with the speed of the flow center-of-mass in the downslope direction at the end
179 of the propagation of the flow, when flow motion direction is mostly downslope.

180 However, these experiments were performed using particles of only one diameter
181 $d = 2$ mm, and the released granular columns had only one mass $M = 77.4$ g and as-

182 pect ratio $a = 0.8$ (i.e. height over diameter of the column). The conclusions of this
183 last paper may then only apply for this specific set of parameters. Therefore, in the present
184 paper, we pursue the work initiated by *Farin et al.* [2018] by releasing 3D granular columns
185 of various particle diameters d , masses M and aspect ratios a . Note that all particles have
186 the same diameter in our experiments. The effect of various particle distributions, as well
187 as the effect of a complex bed shape and presence of an erodible bed are not explicitly
188 explored in this study but would be useful to investigate in future works to better un-
189 derstand the complexities encountered on the field that we mentioned earlier. The spe-
190 cific questions we would like to address are: (1) Are the observations of *Farin et al.* [2018]
191 still valid for different particle diameters, column masses and aspect ratios? (2) Can we
192 establish clear empirical scaling laws relating the absolute radiated seismic energy W_{el} ,
193 the seismic efficiency (ratio of W_{el} over total potential energy lost or over maximum ki-
194 netic energy) and the frequency of the generated seismic signal to the parameters of the
195 released granular columns? Are these laws modified when the slope angle increases? In
196 particular, does the radiated seismic energy depend on slope angle similarly as the runout
197 distance (inversely proportional to $\tan \delta - \tan \theta$ as in equation (1))? Since the flow be-
198 comes more agitated as slope angle increases, it is interesting to correlate the increase
199 of the radiated seismic energy with the increase of particle agitation in the saltating front.
200 (3) How do the empirical scaling laws compare to previous field observations and to that
201 established for a single particle impact? (4) Finally, what properties of granular flows
202 (particle diameter, mass, speed) can we infer from each characteristic of the radiated seis-
203 mic signal in the field?

204 The paper is organized as follows: In section 2, we present the experimental setup
205 and define the investigated dynamics and seismic flow parameters. In section 3, we com-
206 pare the dynamics of granular flows and the generated seismic signals for different flow
207 parameters and we establish empirical scaling laws. The results are interpreted in sec-
208 tion 4 and compared with observations for a single particle impact and in the field. Based
209 on our observed scaling laws, we also discuss which flow properties are possible to de-
210 duce from high-frequency seismic signals in the field. Finally, section 5 presents the con-
211 clusions and perspectives.

2 Experimental Setup and Definition of Flow and Seismic Parameters

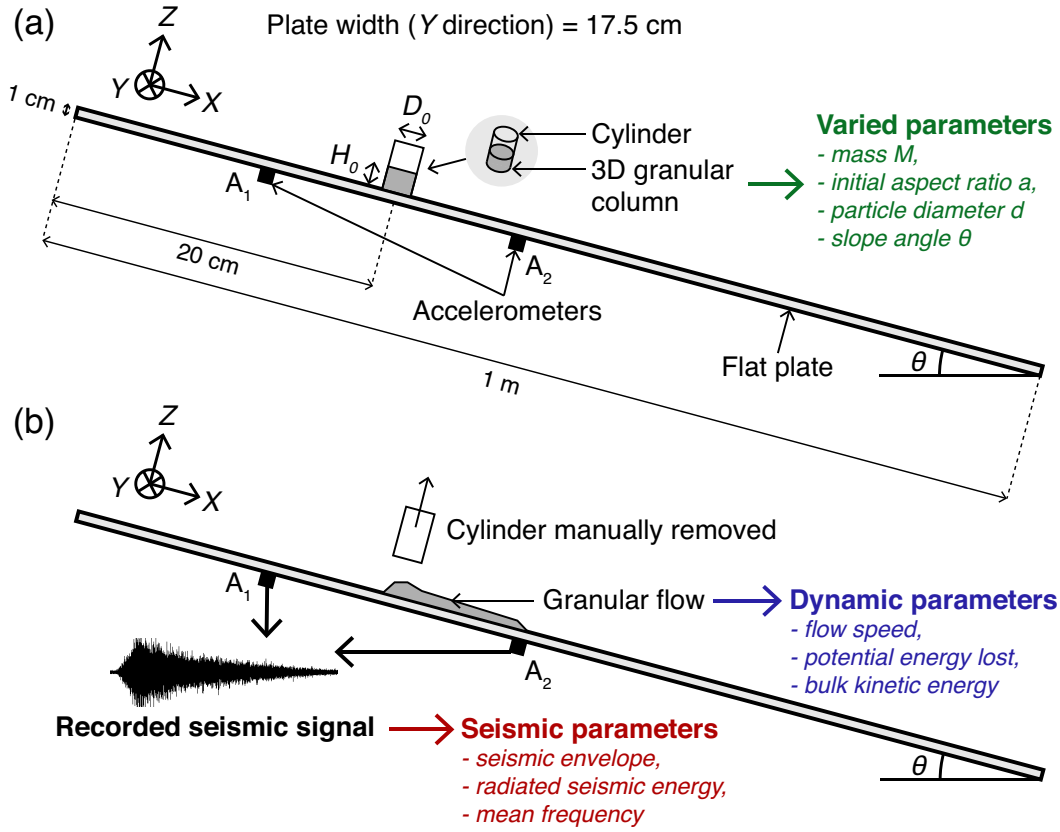
2.1 Experimental Setup

The experimental setup is the same as the one introduced by *Farin et al.* [2018] (Fig. 1). Cylindric granular columns with various initial conditions are suddenly released on a PMMA (Polymethyl methacrylate) plate of thickness $h = 1$ cm. The columns are composed of spherical steel particles of density 7800 kg m^{-3} and of same diameter d . The friction angle of the granular material is $\delta = 27^\circ$. A layer of 2-mm steel beads is glued on the plate surface to create basal roughness and ensure the granular flows form a deposit on the plate when it is inclined. *Farin et al.* [2018] investigated only one column mass $M = 77.4$ g, initial aspect ratio $a = H_0/D_0 = 0.8$ (where H_0 and D_0 are the column's initial height and diameter) and particle diameter $d = 2$ mm for different slope angles $\theta = 0^\circ - 20^\circ$ on the resulting flow dynamics and generated seismic signal. In this paper, we conduct several series of experiments for which one parameter M , a , d and θ is varied while the others are fixed. Table 1 sums up the range of parameters investigated. Note that only the effect of the column mass M (for a fixed aspect ratio $a = 0.8$) and of the aspect ratio a (for a fixed mass $M = 70$ g) are investigated when the slope angle θ increases. An additional series of granular column collapse experiments is also conducted on a thick marble block in order to observe the influence of the substrate (thin plate or thick block) on the relations between seismic and initial columns parameters (see Appendix A:).

A video camera recording 500 frames per second is installed along the side of the granular flow in order to capture the flow dynamics. This recording speed is sufficient to track the motion of individual particles rebounding in front of the flow. In parallel, the seismic vibration generated by the granular flows is measured with using two mono-component piezoelectric accelerometers (type 8309, *Brüel & Kjaer*). The response of these sensors is flat between 1 Hz and 54 kHz. This experimental setup allows us to observe how the properties of the seismic signal (radiated seismic energy, seismic envelope, frequencies) are related to the dynamics and deposit characteristics of the granular flows (potential and kinetic energy, flow speed and acceleration, total flow duration and runout distance) for various initial conditions. Let us first define the dynamics and seismic parameters that we compare in the following sections.

Table 1. Characteristics of the 3D granular columns released on the PMMA plate. When various column initial heights H_0 are given, they correspond to the variation of either the mass M or the aspect ratio a .

d (mm)	M (g)	a (-)	H_0 (cm)	θ ($^\circ$)
2	11.1, 30.9, 37.8, 53	0.4	0.79, 1.11, 1.18, 1.32	0
	16.6, 46.4, 56.7, 79.5	0.6	1.18, 1.67, 1.77, 2	
	22.2, 61.8, 75.6, 105.9, 246.5	0.8	1.58, 2.22, 2.36, 2.65, 3.52	
	27.7, 77.3, 94.5, 308.1	1	2, 2.78, 2.95, 4.4	
2	50	0.16, 0.38, 0.53, 0.65, 1.82	0.7, 1.25, 1.56, 1.8, 3.55	0
	70	0.22, 0.53, 0.74, 0.9	1, 1.75, 2.18, 2.5	
	90	0.28, 0.66, 0.95, 1.11	1.25, 2.2, 2.8, 3.2	
	110	0.36, 0.81, 1.12, 1.37	1.6, 2.7, 3.3, 3.8	
1, 1.58, 2, 2.38, 3.17	126 ± 0.3	0.4	1.76	0
	189 ± 0.3	0.6	2.64	
	100 ± 2	0.75	3	
	132.5 ± 0.2	1	3.31	
2	22.7, 64.4, 77.4, 107.7, 246.1	0.8	1.58, 2.22, 2.36, 2.65, 3.52	0, 5, 10, 15, 20
	70	0.23, 0.52, 0.72, 0.87	1, 1.72, 2.13, 2.42	



232 **Figure 1.** Schematic of the experimental setup (Modified from [Farin et al., 2018]). (a) A
 233 granular column is initially contained in a cylinder on a flat plate inclined at slope angle θ . The
 234 granular column has an initial height H_0 and diameter D_0 , a mass M and initial aspect ratio
 235 $a = H_0/D_0$ and is composed of spherical steel particles of diameter d . (b) The cylinder is sud-
 236 denly removed and the granular column spreads down the slope. The dynamics of the granular
 237 flow (flow speed, potential energy lost, bulk kinetic energy) is recorded along the side using
 238 a video camera and the seismic signal generated by the flow is measured by two piezoelectric
 239 accelerometers (A_1 and A_2) attached to the bottom of the plate.

2.2 Dynamic Parameters

We deduce the dynamic parameters from the time evolution of the flow contour profile $H(X, t)$ evaluated from the successive pictures of the granular flows in the (X, Y, Z) frame linked to the plate (Fig. 2a).

The potential energy lost by the granular flow as a function of time t is

$$\Delta E_p(t) = E_p(t = 0) - E_p(t), \quad (2)$$

with the potential energy $E_p(t)$ computed using the following expression demonstrated by *Farin et al.* [2018]

$$E_p(t) \simeq \frac{1.5}{2} \rho g D_0 \left(\frac{1}{2} \int_X H(X, t)^2 \cos \theta dX - \int_X H(X, t) X \sin \theta dX \right), \quad (3)$$

where $\rho = M/(\pi D_0^2 H_0/4) \simeq 4800 \text{ kg m}^{-3}$ is the average density of the granular flow, g is the gravitational acceleration and D_0 is the initial column diameter.

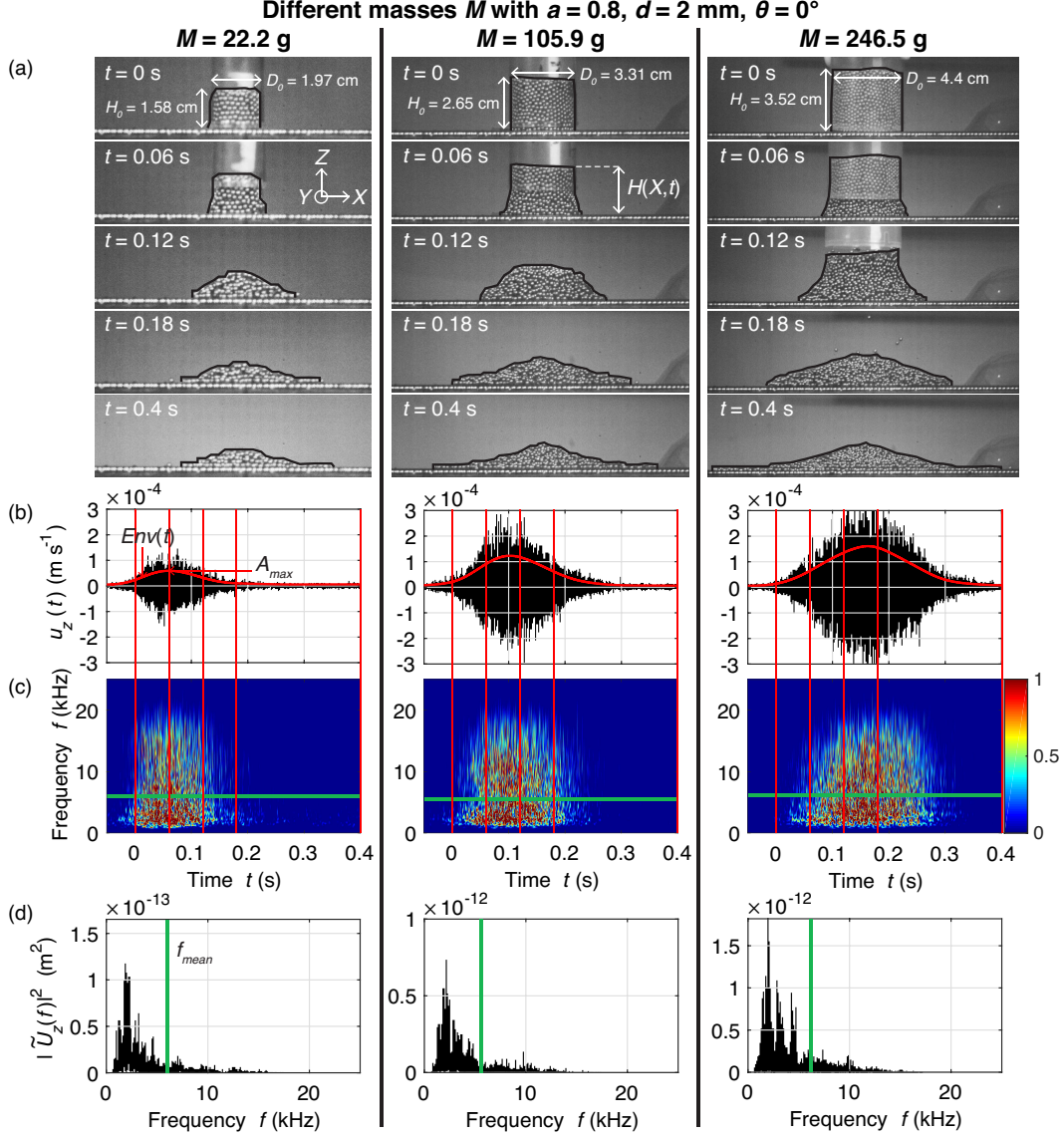
Since most of granular flow motion is in the plane $(X, Y = 0, Z)$, we neglect flow motion in the Y -direction. The coordinates $(X^{COM}(t), Z^{COM}(t))$ of the flow center of mass are obtained by integration of the flow profile $H(X, t)$ along the X and Z -directions, respectively (see *Farin et al.* [2018] for details on the computations of these coordinates). Time derivation of these coordinates gives the bulk speeds $V_X^{COM}(t)$ and $V_Z^{COM}(t)$ in X and Z -directions and the total bulk speed $V_{tot}^{COM}(t) = \sqrt{V_X^{COM}(t)^2 + V_Z^{COM}(t)^2}$. The bulk kinetic energy $E_k(t)$ of the flow is then defined as

$$E_k(t) = \frac{1}{2} M V_{tot}^{COM}(t)^2, \quad (4)$$

and the total energy lost by the granular flow at time t is

$$E_{tot}(t) = \Delta E_p(t) + E_k(t) \quad (5)$$

It is unclear whether the high-frequency seismic amplitude generated by granular flows is more controlled by the motion of the center of mass or by the motion of the flow snout, which propagates faster (and thus is more energetic) than the flow rear. Therefore, we also measure the speed $V_{front}(t)$ of the front of the granular flows and that of the column's summit (towards the plate in the Z -direction) $V_{summit}(t)$.



255 **Figure 2.** (a) Successive pictures of three horizontal ($\theta = 0^\circ$) 3D granular column collapse
 256 experiments with different masses $M = 22.2$ g, $M = 105.9$ g and $M = 246.5$ g, all with initial
 257 column aspect ratio $a = 0.8$ and particle diameter $d = 2$ mm. The black lines show the con-
 258 tours $H(X,t)$ of the granular flows that are used to compute the flow dynamic parameters. (b)
 259 Seismic signals (i.e. plate vibration speed $u_z(t)$) generated by the granular flows as a function of
 260 time t . The red line represent the amplitude envelope, filtered below 5 Hz. (c) Spectrograms of
 261 the signals. Warmer colors mean more energy (normalized to 1). (d) Squared amplitude spectra
 262 $|\tilde{U}_z(f)|^2$ of the seismic signals. The vertical red lines in panels (b) and (c) indicate the times of
 263 the pictures in (a) and the thick green line in panels (c) and (d) indicates the mean frequency
 264 f_{mean} of the signals.

2.3 Seismic Parameters

The two accelerometers attached to the plate measure the acceleration $a_Z(t)$ of the plate surface in the Z -direction generated by the granular flows. We integrate $a_Z(t)$ to obtain the speed $u_Z(t)$ of the plate vibration, that we call the ‘seismic signal’ in the following (Fig. 2b). *Farin et al.* [2018] showed that both accelerometers measure the same seismic amplitude because the seismic waves emitted by the granular flows are reflected many times off the boundaries of the plate and the radiated seismic energy is rapidly equipartitioned within the plate. We are therefore confident that an increase in the seismic amplitude reflect a change in the dynamics of the granular flows and not the fact that the flow gets closer to the accelerometer.

We characterize the seismic signal by its seismic envelope $Env(t)$ and its maximum value A_{max} (Fig. 2b). A Fourier transform of the seismic signal $u_Z(t)$ gives the spectrogram and the amplitude spectrum $|\tilde{U}_Z(f)|$ (Fig. 2cd). We characterize the amplitude spectrum with its average frequency defined as

$$f_{mean} = \frac{\int_0^{+\infty} |\tilde{U}_Z(f)| f df}{\int_0^{+\infty} |\tilde{U}_Z(f)| df}. \quad (6)$$

We choose to use the mean frequency rather than, for example, the maximum frequency of the spectrum because it averages the contributions of all of the particles impacting the bed during the granular flow. Indeed, each impact of the particles during the granular flow has a slightly different duration, which results in a slightly wider or less wide frequency spectrum. By taking the average frequency, we take the average of the frequency spectra of all impacts.

The seismic parameter we are most interested in is the absolute energy W_{el} radiated in the form of elastic waves by the granular flows because, in the field, this parameter does not depend on the distance between the source and the seismic station and can quantitatively be compared with the potential energy lost ΔE_p and the kinetic energy E_k of the granular flows [e.g. *Vilajosana et al.*, 2008; *Hibert et al.*, 2011; *Lévy et al.*, 2015; *Hibert et al.*, 2017c]. As discussed by *Farin et al.* [2018], the normal motion $u_Z(t)$ measured at one location of the plate surface is sufficient to evaluate $W_{el}(t)$. Indeed, in the frequency range of interest (1–20 kHz), the only mode excited in the plate is the flexural mode A_0 which has a displacement normal to the plate surface [*Royer and Dieulesaint*, 2000]. *Farin et al.* [2018] demonstrated a method to evaluate the radiated seismic energy $W_{el}(t)$ in this experimental context, which is different than classical techniques

319 used for rockfalls and landslides in the field [e.g. *Vilajosana et al.*, 2008; *Hibert et al.*,
 320 2011; *Lévy et al.*, 2015; *Hibert et al.*, 2017c]

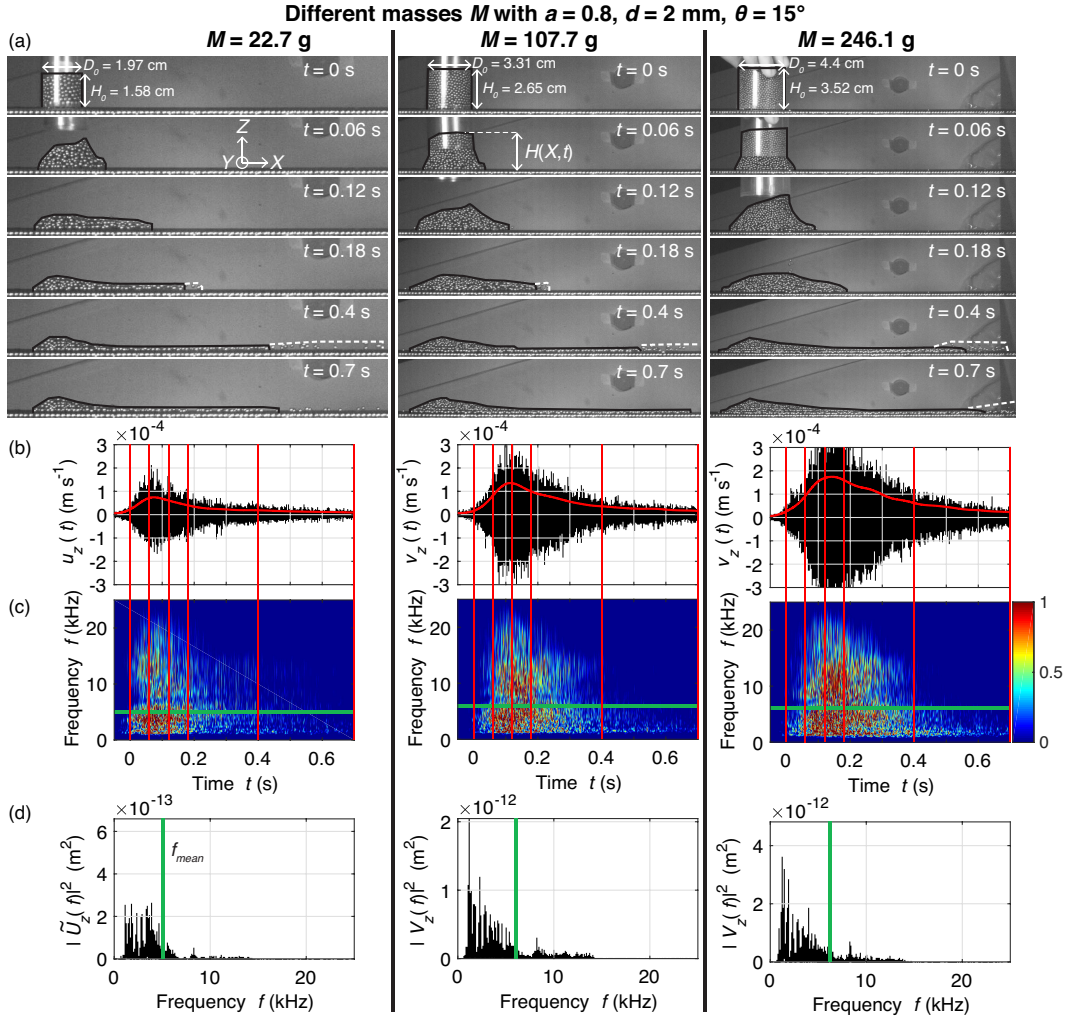
$$321 \quad W_{el}(t) \approx \frac{\rho_p V_p}{\tau} \int_0^t u_Z(t')^2 dt', \quad (7)$$

322 where $u_Z(t)$ is the seismic signal, ρ_p and V_p are the density and volume of the plate, re-
 323 spectively and τ is the characteristic time of energy dissipation in the plate, which de-
 324 pends on frequency [*Farin et al.*, 2016]. The total seismic energy radiated during the whole
 325 experiment is then $W_{el} = W_{el}(t_s)$, where t_s is the duration of the seismic signal.

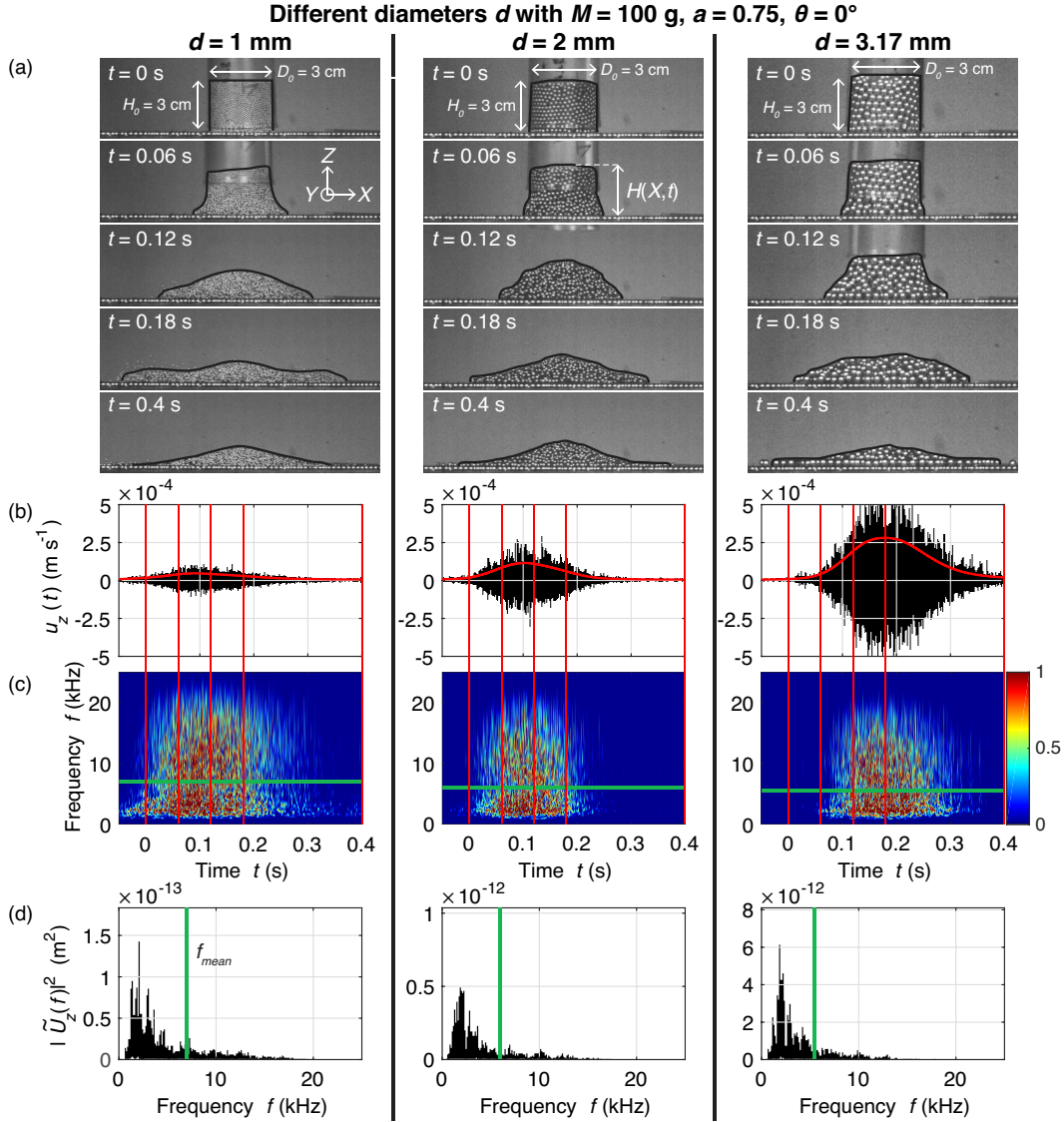
326 **3 Comparison of the Seismic and Dynamic Parameters**

327 **3.1 Description of the Seismic Signals**

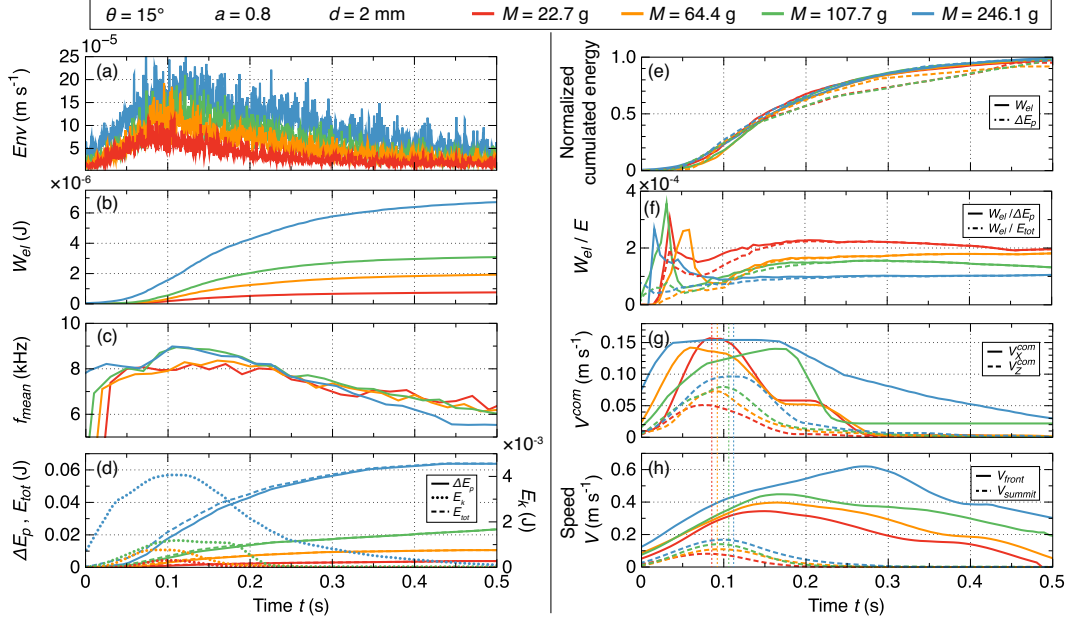
328 The seismic signals generated by the granular column collapses have an emergent
 329 rise and long decay (Fig. 2b, 3b and 4b) and compare well with seismic signals of land-
 330 slides and rockfalls observed in the field [*Schneider et al.*, 2010; *Dammeier et al.*, 2011;
 331 *Hibert et al.*, 2011; *Moretti et al.*, 2012; *Hibert et al.*, 2014b; *Pérez-Guillén et al.*, 2016].
 332 Similarly as was previously reported by *Farin et al.* [2018], on an horizontal slope the
 333 shape of the seismic envelope is symmetrical with respect to its maximum. As the slope
 334 angle θ increases, the duration of decay phase increases with respect to that of the rise
 335 phase because the flow takes a longer duration to decelerate as the importance of grav-
 336 ity increases over frictional forces. At high slope angles, the decay phase is much more
 337 elongated than the rise phase (for example compare Fig. 2b for $\theta = 0^\circ$ with Fig. 3b
 338 for $\theta = 15^\circ$). Interestingly, this dependence of the signal shape to slope angle is observed
 339 regardless of the column mass M or initial aspect ratio a (Fig. 2bc and 3bc for the mass
 340 M ; see Appendix B: , Fig. B.1 and B.2 for the aspect ratio a). We think that this change
 341 of shape is related to a change of the flow regime from a dense flow to a diluted and ag-
 342 itated flow, with a front of particles saltating on the bed which is not observed at small
 343 slope angles θ (see Fig. 3a for $t > 0.18$ s) [*Farin et al.*, 2018]. Regardless of the flow
 344 parameters, the granular flows generate a signal of frequencies between 1 kHz and 20 kHz
 345 (Fig. 2cd, 3cd and 4cd). Effects of flow parameters on the average frequency f_{mean} is
 346 discussed in section 3.3.



347 **Figure 3.** Same as Fig. 2 but when the plate is inclined at slope angle $\theta = 15^\circ$. The white
 348 dashed line in (a) shows the contour of the assembly of saltating particles at the front of the
 349 granular flow.



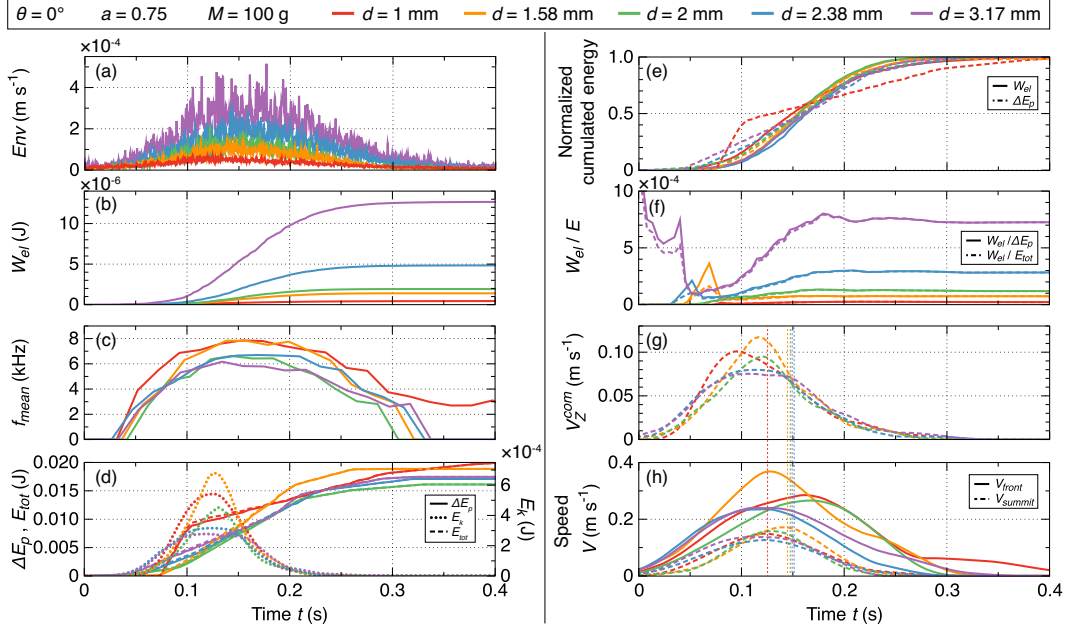
350 **Figure 4.** (a) Successive pictures of three horizontal ($\theta = 0^\circ$) granular column collapse exper-
351 iments with different particle diameter $d = 1$ mm, $d = 2$ mm and $d = 3.17$ mm, all with initial
352 column aspect ratio $a = 0.75$ and mass $M = 100$ g. The black lines show the contours $H(X, t)$
353 of the granular flows that are used to compute the flow dynamic parameters. (b) Seismic signals
354 (i.e. plate vibration speed $u_z(t)$) generated by the granular flows as a function of time t . The
355 red line represent the amplitude envelope, filtered below 5 Hz. (c) Spectrograms of the signals.
356 Warmer colors mean more energy (normalized to 1). (d) Squared amplitude spectra $|\tilde{U}_Z(f)|^2$ of
357 the seismic signals. The vertical red lines in panels (b) and (c) indicate the times of the pictures
358 in (a) and the thick green line in panels (c) and (d) indicates the mean frequency f_{mean} of the
359 signals.



366 **Figure 5.** Comparison of the dynamics of granular flows with the generated seismic signal
 367 for $\theta = 15^\circ$, $a = 0.8$, $d = 2$ mm and different column masses M (different colors). (a) En-
 368 velope $Env(t)$ of the seismic signal filtered below 100 Hz. (b) Radiated seismic energy $W_{el}(t)$.
 369 (c) Mean frequency f_{mean} . (d) Potential energy lost ΔE_p , kinetic energy E_k and total energy
 370 $E_{tot} = \Delta E_p + E_k$. (e) Normalized cumulated radiated seismic energy $W_{el}(t)$ and potential energy
 371 lost ΔE_p . (f) Ratio of the radiated seismic energy over the potential energy lost and the total
 372 energy lost. (g) Speeds V_X^{COM} and V_Z^{COM} of the flow center-of-mass in the X and Z -directions,
 373 respectively. (h) Speed V_{front} and V_{summit} of the flow front (in X -direction) and of the flow sum-
 374 mit (in Z -direction). In panels (g) and (h), the vertical dashed lines indicate the maximum of the
 375 envelope $Env(t)$ of the seismic signal.

3.2 Temporal Comparison of Flow Dynamics with Seismic Signal

360
 361 The temporal variation of the seismic and dynamic characteristics is compared for
 362 different masses M at slope angle $\theta = 15^\circ$ in Fig. 5 and for different particle diame-
 363 ters d at $\theta = 0^\circ$ in Fig. 6 (see Appendix B: , Fig. B.3 for different masses M at $\theta =$
 364 0° and Fig. B.4 and B.5 for different aspect ratios a). The quantitative influence of these
 365 parameters on seismic signal characteristics is discussed in the next section 3.3.



376 **Figure 6.** Same as Fig. B.3 but for $\theta = 0^\circ$, $a = 0.75$, $M = 100$ g and different particle diameters d (different colors).
377

378 The observations of *Farin et al.* [2018] for one set of parameters M , a and d and
379 different slope angles θ remain true for various masses M , aspect ratios a and particle
380 diameters d . Mainly:

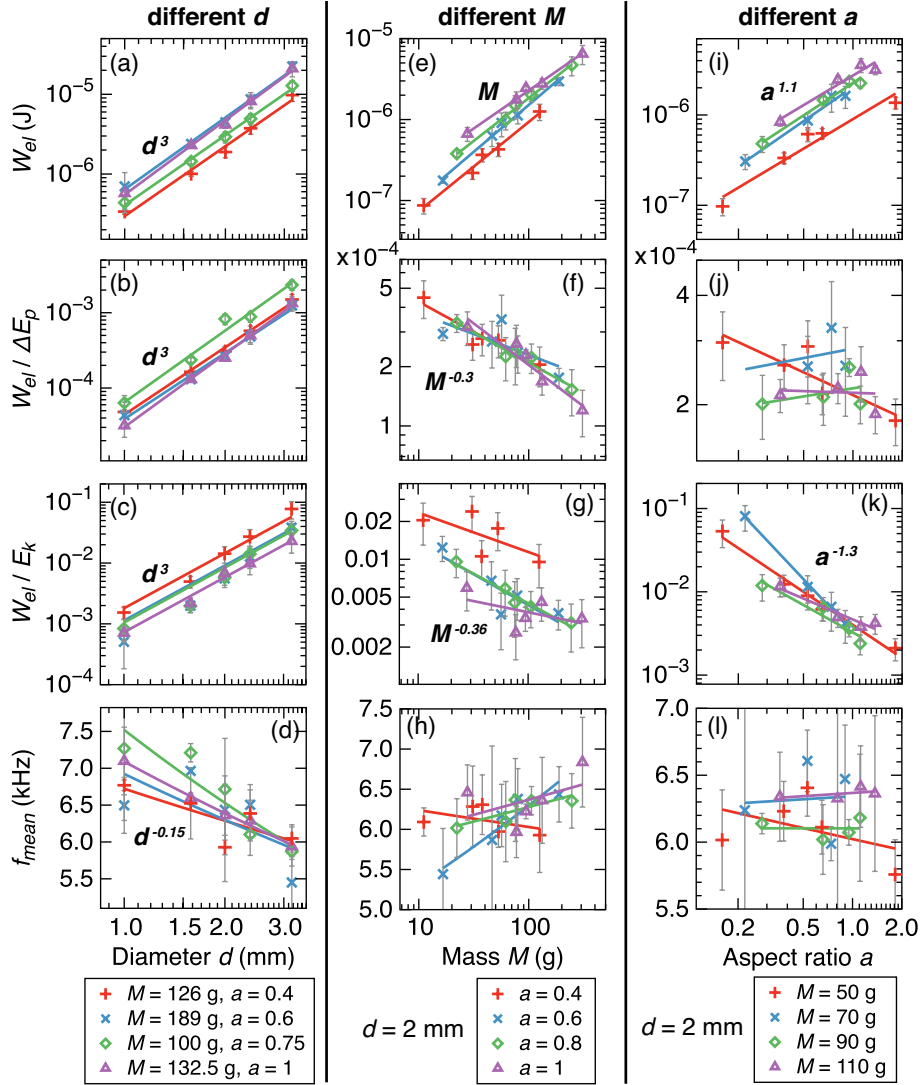
- 381 1. The maximum seismic amplitude coincides well with the maximum flow speed in
382 the Z -direction (e.g. compare maximum $Env(t)$, indicated by vertical dashed lines,
383 with the speeds V_Z^{COM} and V_{summit} for Fig. 5agh). In contrast, the seismic am-
384 plitude does not match with flow motion in the X -direction during the rise phase
385 but starts depending on motion in this direction during the deceleration phase when
386 flow motion in the Z -direction has stopped (e.g. compare maximum $Env(t)$ with
387 the speeds V_X^{COM} and V_{front} for 5agh).
- 388 2. The time variation of the radiated seismic energy $W_{el}(t)$ and the potential energy
389 lost $\Delta E_p(t)$ is similar and their normalized profiles match well (Fig. 5bde and 6bde).
390 Same observations can be made when comparing W_{el} with the total energy lost
391 E_{tot} because the bulk kinetic energy E_k is much smaller than the potential energy
392 lost $\Delta E_p(t)$, so that $E_{tot} \approx \Delta E_p$ (Fig. 5d and 6d).

- 393 3. The seismic efficiency (i.e. the ratio $W_{el}(t)/\Delta E_p(t)$ or $W_{el}(t)/E_{tot}(t)$) is difficult
394 to evaluate in the rise phase because energies are small but it tends towards a con-
395 stant value in the decay phase (Fig. 5f and 6f). In the next section, we inspect
396 how this final value (at the end of the flow) quantitatively changes when flow pa-
397 rameters vary.
- 398 4. The increase of the duration of the flow deceleration phase when the slope angle
399 θ increases is visible in the shape of the seismic signal amplitude, energy and mean
400 frequency and of the normalized curves of $W_{el}(t)$ and $\Delta E_p(t)$ (with a much longer
401 decay phase than for $\theta = 0^\circ$, Fig. 5abce).

402 3.3 Influence of Granular Column Initial Parameters

403 We now discuss how the particle diameter d , column mass M , initial aspect ratio
404 a and slope angle θ quantitatively affect the total radiated seismic energy W_{el} (for the
405 whole signal duration t_s), the ratio of this energy over the total potential energy lost $\Delta E_p =$
406 $\Delta E_p(t_s)$, and over the maximum kinetic energy $E_k = \frac{1}{2}M \max(V_{tot}^{COM})^2$ and the mean
407 frequency f_{mean} of the total seismic signal (Fig. 7). Data in Fig. 7 are fitted by power
408 laws $Y = bX^c$, and parameters b and c are given in Table 2.

419 The radiated seismic energy W_{el} strongly depends on particle diameter as d^3 , re-
420 gardless of the column's mass M and aspect ratio a (Fig. 7a). In contrast, W_{el} increases
421 approximatively linearly with column's mass as $M^{1.0}$ and column's initial aspect ratio
422 as $a^{1.1}$ (Fig. 7ei). Increasing the particle diameter d while keeping all other parameters
423 (M, a, θ) unchanged does not affect the bulk flow dynamics (i.e. $\Delta E_p, E_k$ and flow bulk
424 speeds), but it only increases the radiated seismic energy W_{el} (Fig. 6bdgh). Consequently,
425 the power 3 dependence in particle diameter d is conserved for the ratio of radiated seis-
426 mic energy W_{el} over potential energy lost ΔE_p and maximum kinetic energy E_k (Fig.
427 7bc). On the contrary, varying the column's mass M and aspect ratio a affect the bulk
428 flow dynamics (Fig. 5bdgh and Appendix B:). Both ΔE_p and E_k appear to depend on
429 flow mass as about $M^{1.3}$, so that ratios $W_{el}/\Delta E_p$ and W_{el}/E_k are approximatively pro-
430 portional to $M^{-0.3}$ (Fig. 7fg). The dependence of W_{el} and ΔE_p on aspect ratio a is ap-
431 proximately the same, so that the ratio $W_{el}/\Delta E_p$ does not depend on a (Fig. 7j). In con-
432 trast, the kinetic energy E_k strongly depends on aspect ratio a , at least at power 2.3,
433 because higher a imply higher heights of fall of the particles and higher maximum flow
434 speeds, and consequently $W_{el}/E_k \propto a^{-1.3}$ (Fig. 7k). We have strong uncertainties (\sim



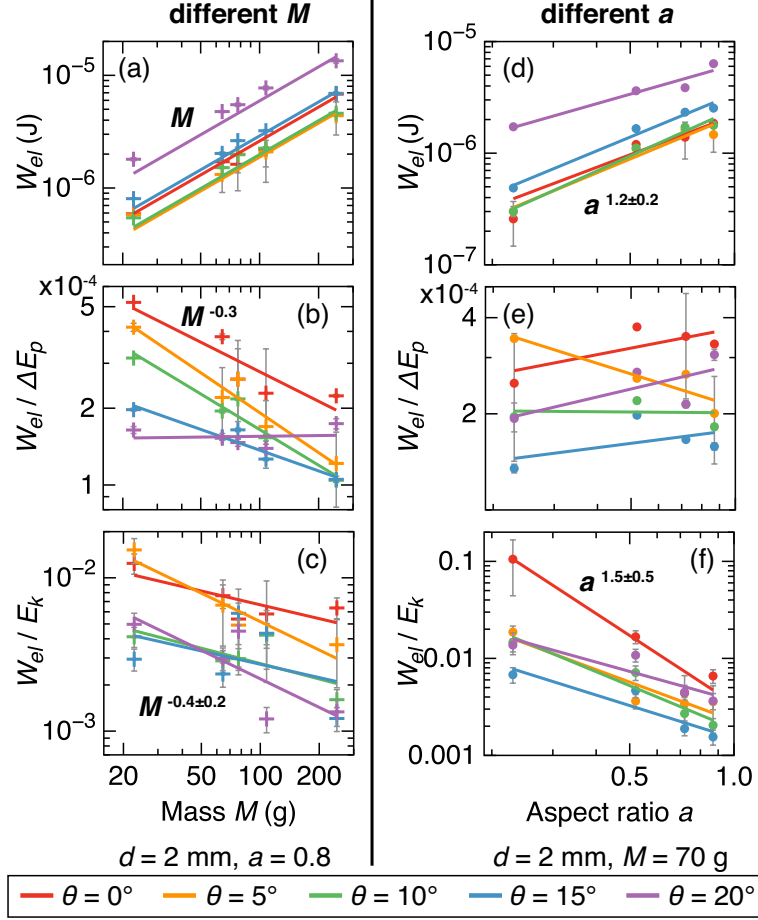
409 **Figure 7.** Seismic parameters as a function of the granular column parameters for the experi-
 410 ments on the PMMA thin plate. (a),(e),(i) Radiated seismic energy W_{el} , (b),(f),(j) Ratio of W_{el}
 411 over the potential energy lost ΔE_p , (c),(g),(k) Ratio of W_{el} over the total kinetic energy ΔE_k ,
 412 (d),(h),(l) Mean frequency f_{mean} of the seismic signal for (a) to (d) different particle diameter d
 413 for various couples of fixed column mass M and initial aspect ratios a , (e) to (h) different masses
 414 M for $d = 2$ mm and fixed aspect ratios a and (i) to (l) different aspect ratios a for $d = 2$ mm
 415 and fixed masses M . Data are fitted by power laws (full lines). The power law is indicated when
 416 a tendency is observed (see Table 2 for details).

417 **Table 2.** Power laws $Y = bX^c$ used to fit the data in Fig. 7 and uncertainties Δb and Δc on
 418 parameters b and c . Coefficients are given in S.I. units.

$Y = bX^c$	Δb	Δc	R^2
$W_{el} = 4.7 \cdot 10^2 d^{3.0}$	$\pm 1.5 \cdot 10^2$	± 0.1	0.99
$W_{el} = 2.1 \cdot 10^{-5} M^{1.06}$	$\pm 1.7 \cdot 10^{-5}$	± 0.09	0.99
$W_{el} = 2.0 \cdot 10^{-6} a^{1.14}$	$\pm 0.8 \cdot 10^{-6}$	± 0.08	0.96
$W_{el}/\Delta E_p = 4.4 \cdot 10^4 d^{3.0}$	$\pm 1.5 \cdot 10^4$	± 0.2	0.99
$W_{el}/\Delta E_p = 1.2 \cdot 10^{-4} M^{-0.3}$	$\pm 4.3 \cdot 10^{-5}$	± 0.09	0.82
$W_{el}/\Delta E_p = 2.3 \cdot 10^{-4} a^{-0.01}$	$\pm 0.3 \cdot 10^{-4}$	± 0.13	0.24
$W_{el}/E_k = 7.7 \cdot 10^5 d^{3.0}$	$\pm 3.8 \cdot 10^5$	± 0.2	0.95
$W_{el}/E_k = 2.6 \cdot 10^{-2} M^{-0.36}$	$\pm 1.3 \cdot 10^{-2}$	± 0.15	0.6
$W_{el}/E_k = 3.8 \cdot 10^{-3} a^{-1.3}$	$\pm 0.6 \cdot 10^{-3}$	± 0.5	0.96
$f_{mean} = 2.55 \cdot 10^3 d^{-0.15}$	± 100	± 0.04	0.71
$f_{mean} = 6.6 M^{0.027}$	± 0.96	± 0.036	0.48
$f_{mean} = 6.2 a^{-0.002}$	± 0.2	± 0.012	0.37

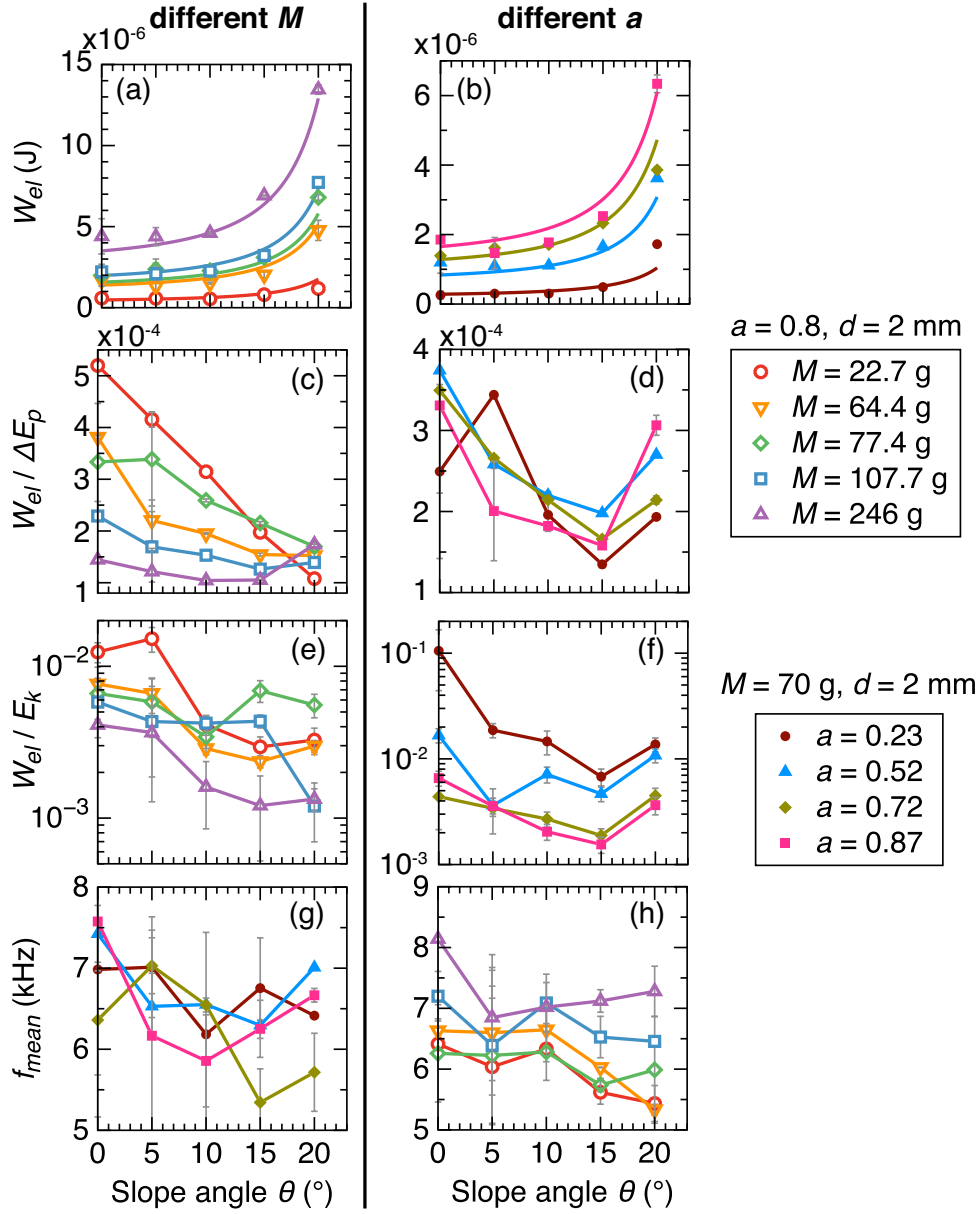
435 20%) on the data of the mean frequency f_{mean} , which makes it difficult to draw conclu-
 436 sions from these data, especially as a function of M and a (Fig. 7dhl). The variation of
 437 f_{mean} as a function of the particle diameter d is slightly larger than the error bars and
 438 we can note a small decrease of f_{mean} as $d^{-0.15}$.

439 The power in the scaling laws as a function of mass M and aspect ratio a is only
 440 slightly modified when the slope angle θ increases (Fig. 8). The apparent independence
 441 of $W_{el}/\Delta E_p$ on mass M for $\theta = 20^\circ$ (purple line, Fig. 8b) may be due to the fact that
 442 we underestimated ΔE_p for the large mass $M = 246.5$ g since the front of the flow prop-
 443 agated outside of the camera view. Contrary to the power coefficient, the value of the
 444 proportionality coefficient in the scaling laws significantly changes as slope angle θ in-
 445 creases. Indeed, regardless of M and a , the radiated seismic energy W_{el} increases when
 446 the slope angle θ increases, but only after a critical slope angle θ , between 10° and 15°
 447 (Fig. 8ab and 9ab). The increase is stronger as θ approaches the friction angle $\delta = 27^\circ$.
 448 We further discuss this dependence in section 4.1. The ratios $W_{el}/\Delta E_p$ and W_{el}/E_k glob-
 449 ally decrease as slope angle θ increases until $\theta = 20^\circ$ for which the ratios increase again



457 **Figure 8.** Influence of the slope angle θ (different colors) of the PMMA plate on the scaling
 458 laws of seismic parameters with mass M and aspect ratio a . (a),(d) Radiated seismic energy W_{el} ,
 459 (b),(e) Energy ratio $W_{el}/\Delta E_p$ and (c),(f) Energy ratio W_{el}/E_k , for (a) to (c) $d = 2$ mm, $a = 0.8$
 460 and different masses M and (d) to (f) $d = 2$ mm, $M = 70$ g and different aspect ratios a . Data
 461 are fitted by power laws (full lines).

450 for some experiments (Fig. 9cdef). This observed increase for high slope angles θ may
 451 be related to the change of dynamic regime of the granular flows when a saltating front
 452 appears at the flow front. The individual saltating particles could radiate higher seis-
 453 mic energy W_{el} at impact while barely contributing to the bulk potential energy and ki-
 454 netic energy of the flow, causing the ratios $W_{el}/\Delta E_p$ and W_{el}/E_k to increase. We ob-
 455 serve a slight decrease of the mean frequency f_{mean} as slope angle θ increases in some
 456 cases, but the variation is within the error bars (Fig. 9gh).



462 **Figure 9.** Seismic parameters as a function of the slope angle θ for the experiments on the
 463 PMMA plate. (a),(b) Radiated seismic energy W_{el} . (c),(d) Ratio of W_{el} over the potential energy
 464 lost ΔE_p . (e),(f) Ratio of W_{el} over the total kinetic energy E_k . (g),(h) Mean frequency f_{mean} of
 465 the seismic signal for (a),(c),(e),(g) $d = 2$ mm, $a = 0.8$ and different masses M (different colors)
 466 and (b),(d),(f),(h) $d = 2$ mm, $M = 70$ g and different aspect ratios a . Data of W_{el} in panels
 467 (a) and (b) are fitted by the function $2.15 \cdot 10^{-3} H_0^2 (0.081 / (\tan \delta - \tan \theta)^2 + 1)$, with H_0 the
 468 column's initial height and $\delta = 27^\circ$, the friction angle of the granular material (see section 4.1 for
 469 explanations).

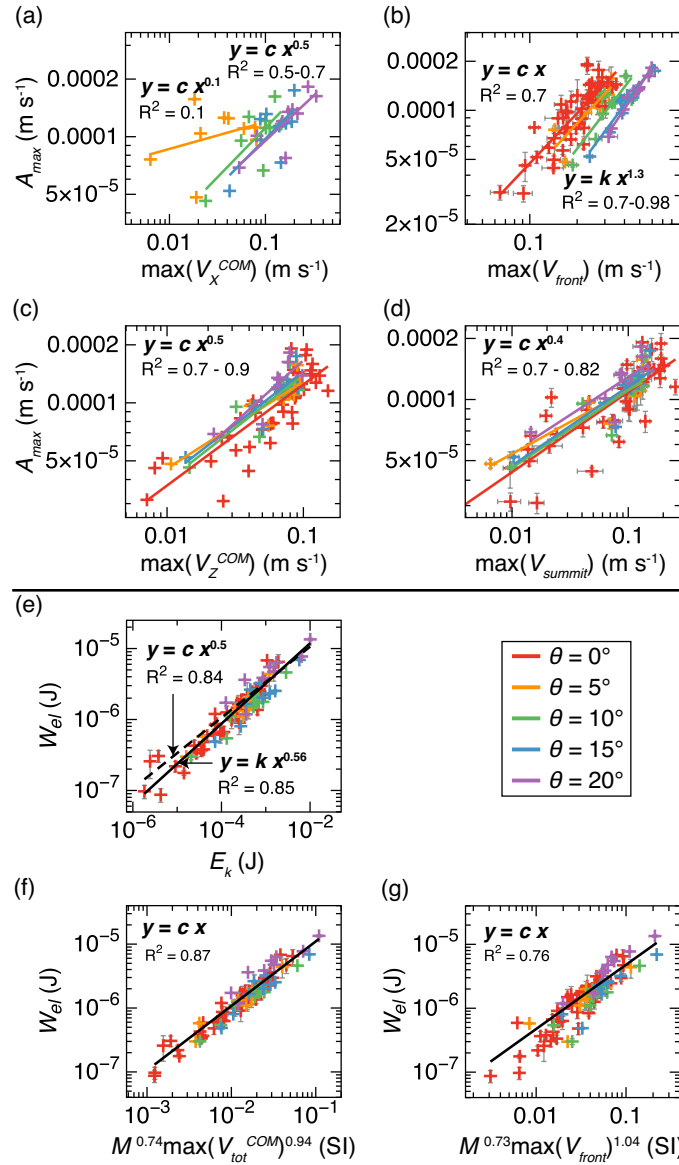
486 **Table 3.** Power laws $Y = bX^c$ used to fit the data in Fig. 10 and 11 and uncertainties Δb and
 487 Δc on parameters b and c . Coefficients are given in S.I. units.

$Y = bX^c$	Δb	Δc	R^2
$2.8 \cdot 10^{-4} \max(V_X^{COM})^{0.4}$	$\pm 8.5 \cdot 10^{-5}$	± 0.2	0.46
$5.1 \cdot 10^{-4} \max(V_Z^{COM})^{0.55}$	$\pm 1.7 \cdot 10^{-4}$	± 0.086	0.77
$4.2 \cdot 10^{-4} \max(V_{front})^{1.21}$	$\pm 5.5 \cdot 10^{-5}$	± 0.18	0.8
$2.7 \cdot 10^{-4} \max(V_{summit})^{0.37}$	$\pm 2.5 \cdot 10^{-5}$	± 0.03	0.75
$10^{-4} E_k^{0.5}$	–	–	0.84
$1.6 \cdot 10^{-4} E_k^{0.56}$	–	–	0.85
$1.3 \cdot 10^4 d^3 M^{0.74} \max(V_{tot}^{COM})^{0.94}$	–	–	0.87
$6 \cdot 10^3 d^3 M^{0.73} \max(V_{front})^{1.04}$	–	–	0.76

470 3.4 Relations Between Dynamics and Seismic Parameters

471 It is interesting to compare the maximum amplitude A_{max} and radiated seismic
 472 energy W_{el} of the seismic signal generated by a granular flow with the maximum flow
 473 speed of the front and of the center of mass in both X and Z -directions, in order to bet-
 474 ter understand which flow dynamic parameters has the most influence on the generated
 475 seismic signal, and thus could be extrapolated from the high-frequency seismic signal in
 476 the field (Fig. 10). The observed scaling laws are summed up in Table 3 (Normalized
 477 laws for W_{el} are given in Appendix C:).

488 Globally, the maximum seismic amplitude A_{max} matches better in time and am-
 489 plitude with the maximum of the flow speed in the Z -direction than in the X -direction,
 490 as already reported by *Farin et al.* [2018] (Fig. 10a-d, see also section 3.2). We confirm
 491 these observations for various initial parameters M , a and d . Correlation between flow
 492 speed in the X -direction and seismic amplitude A_{max} is higher at high slope angles be-
 493 cause the flow motion spends a longer duration in the X -direction than for small slope
 494 angles (Fig. 10ab). In the X -direction, there is no correlation between the maximum seis-
 495 mic amplitude A_{max} and the maximum speed of the center of mass at the horizontal,
 496 for $\theta = 0^\circ$, because $V_X^{COM} = 0 \text{ m s}^{-1}$ while the seismic amplitude is not null. At high
 497 slope angles, A_{max} increases as $(\max(V_X^{COM}))^{0.5}$. A stronger correlation is observed be-
 498 tween A_{max} and the maximum front speed $\max(V_{front})$ (at power ~ 1.2). In the Z -direction,



478 **Figure 10.** (a) to (d) Maximum amplitude A_{max} of the seismic envelope as a function of (a)
 479 the maximum speed $\max(V_X^{COM})$ of the center of mass in X -direction, (b) the maximum speed
 480 $\max(V_{front})$ of the flow front, (c) the maximum speed $\max(V_Z^{COM})$ of the center of mass in Z -
 481 direction and (d) the maximum speed $\max(V_{summit})$ of the summit. (e) Radiated seismic energy
 482 W_{el} as a function of the maximum kinetic energy E_k . (f) W_{el} as a function of the mass M and
 483 the maximum total speed of the center of mass $\max(V_{tot}^{COM})$. (g) Radiated seismic energy W_{el} as
 484 a function of M and the maximum speed of the flow front $\max(V_{front})$. The different colors are
 485 for different slope angles θ .

499 the maximum envelope amplitude A_{max} matches with the speed of the flow at power of
500 0.4–0.55 for both V_Z^{COM} and V_{summit} , regardless of slope angle θ , with correlation co-
501 efficient $R^2 = 0.75 - 0.77$ (Fig. 10cd).

502 A more relevant speed to compare with the radiated seismic energy W_{el} seems to
503 be the maximum total speed of the center of mass $\max(V_{tot}^{COM})$. Indeed, the radiated
504 seismic energy W_{el} matches well with the square root of the maximum kinetic energy
505 $E_k = \frac{1}{2}M \max(V_{tot}^{COM})^2$, with best fit observed as $E_k^{0.56}$ (Fig. 10e). W_{el} should then
506 approximately increase as $M^{0.5} \max(V_{tot}^{COM})$. However, the best fit of W_{el} with adjustable
507 power coefficients is $M^{0.74} \max(V_{tot}^{COM})^{0.94}$ independently of slope angle θ , with a good
508 correlation coefficient $R^2 = 0.87$ (Fig. 10f). Thus, the radiated seismic energy W_{el} is
509 almost proportional to the maximum total speed of the center of mass $\max(V_{tot}^{COM})$. The
510 reason why W_{el} is not proportional to the column mass M as reported in Fig. 7e may
511 be because $\max(V_{tot}^{COM})$ also slightly depends on M . We also observe a good correla-
512 tion between the radiated seismic energy W_{el} and a function of the column’s mass and
513 the maximum front speed as $M^{0.73} \max(V_{front})^{1.04}$, although with a lower $R^2 = 0.76$
514 than for the relation with $\max(V_{tot}^{COM})$ (Fig. 10g). The fits of Fig. 10fg are for a given
515 particle diameter $d = 2$ mm and we previously observed that $W_{el} \propto d^3$ (Fig. 7a). Con-
516 sequently, for all of our experimental data, the radiated seismic energy W_{el} matches well
517 with the following functions of the flow parameters (with $R^2 \approx 0.8$, Fig. 11ab)

$$518 \quad W_{el} \approx 1.3 \cdot 10^4 d^3 M^{0.74} \max(V_{tot}^{COM})^{0.94}, \quad (8)$$

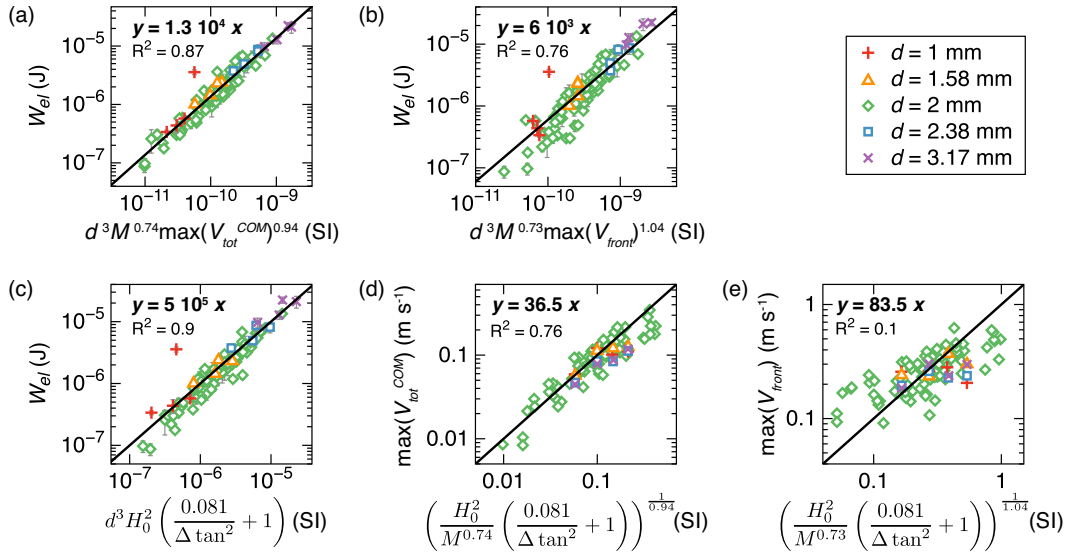
$$519 \quad W_{el} \approx 6 \cdot 10^3 d^3 M^{0.73} \max(V_{front})^{1.04}. \quad (9)$$

520 Since these fits are independent of the column’s initial aspect ratio a and slope angle θ ,
521 the previously observed dependence of the radiated seismic energy W_{el} to a and θ should
522 then be included in the speeds $\max(V_{tot}^{COM})$ and $\max(V_{front})$. We discuss this below.

530 4 Discussion

531 4.1 Dependence on Slope Angle

532 We can interpret the increase of the radiated seismic energy W_{el} and of the max-
533 imum speeds $\max(V_{tot}^{COM})$ and $\max(V_{front})$ as a function of slope angle θ by compar-
534 ing it with the increase of the flow runout distance r_f and flow duration t_f as θ increases.
535 *Mangeney et al.* [2010] showed analytically that the runout distance r_f of granular flow



523 **Figure 11.** (a),(b),(c) W_{el} as a function of (a) $d^3 M^{0.74} \max(V_{tot}^{COM})^{0.94}$, (b)
524 $d^3 M^{0.73} \max(V_{tot}^{COM})^{1.04}$ and (c) $d^3 H_0^2 (0.081 / (\Delta \tan^2 + 1))$, with M , the column mass,
525 V_{tot}^{COM} , the total speed of the center of mass, V_{front} , the front speed, H_0 , the initial column
526 height, θ , the slope angle and δ , the friction angle, for different particle diameter d (different
527 colored symbols). (d) Maximum total speed of the center of mass $\max(V_{tot}^{COM})$ and (e) Maxi-
528 mum speed of the flow front $\max(V_{front})$ as function of H_0 , M and θ for different d . Data are
529 compared with a scaling law $y = cx$, with c , a constant (full line).

564 **Table 4.** Parameters of the scaling laws $Y = c_1/(\tan \delta - \tan \theta)^b + c_2$ used to fit the data in Fig.
 565 12, with δ , the friction angle and θ , the slope angle.

Y	$=$	$c_1/(\tan \delta - \tan \theta)^b + c_2$	R^2
r_f/H_0	$=$	$1.73/(\tan \delta - \tan \theta) - 1.58$	0.98
	$=$	$1.39/(\tan \delta - \tan \theta)$	0.93
t_s/τ_c	$=$	$3.85/(\tan \delta - \tan \theta) - 3.75$	0.95
	$=$	$3.02/(\tan \delta - \tan \theta)$	0.89
W_{el}/H_0^2	$=$	$1.72 \cdot 10^{-4}/(\tan \delta - \tan \theta)^2 + 2.15 \cdot 10^{-3}$	0.99

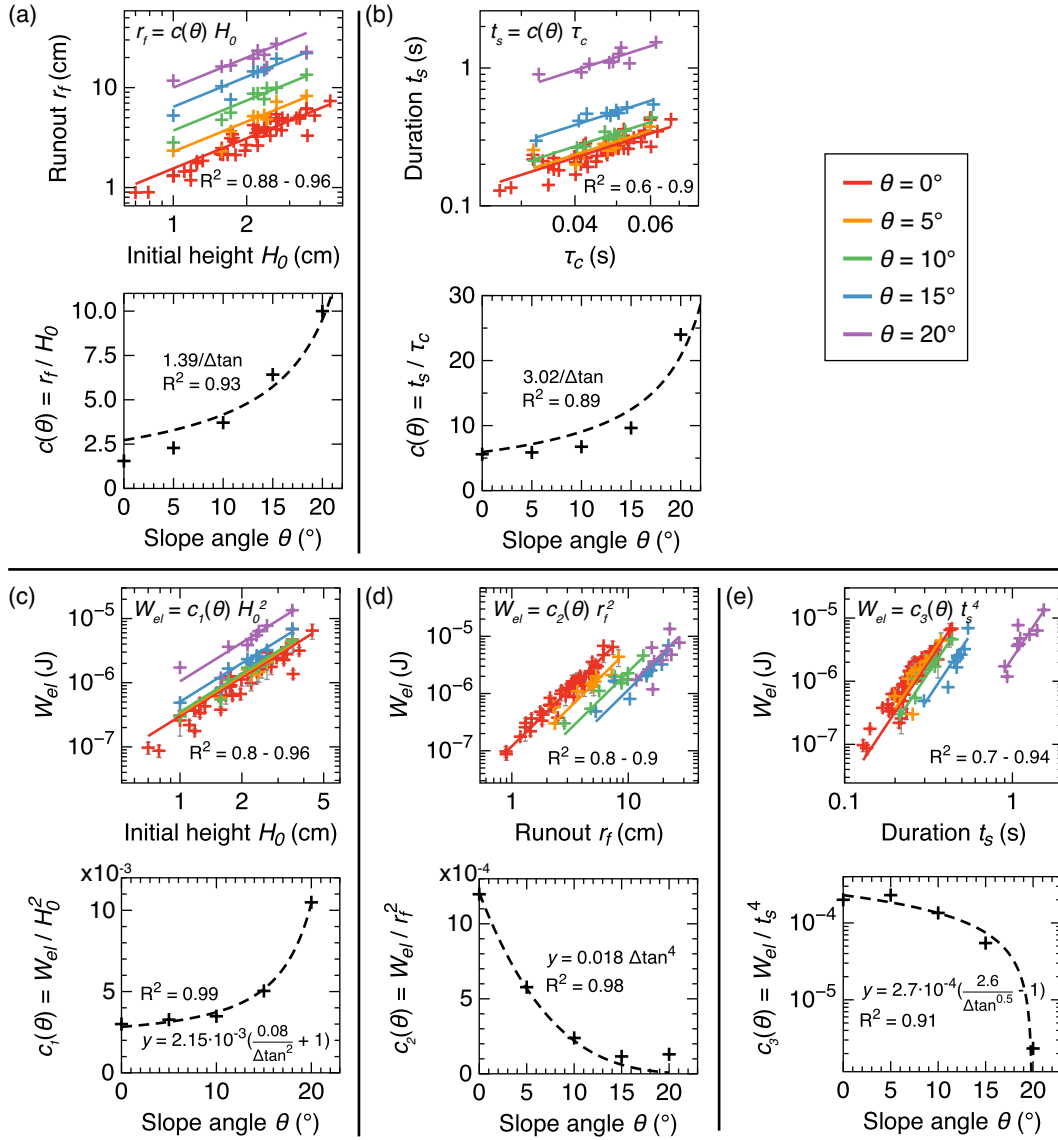
536 and its duration t_f are given by

$$537 \quad r_f = \frac{2kH_0}{\tan \delta - \tan \theta}, \quad (10)$$

$$538 \quad t_f = \frac{2\sqrt{k}\tau_c}{\tan \delta - \tan \theta}, \quad (11)$$

539 with H_0 , the initial height of the granular column, δ , the friction angle of the granular
 540 material, k , a constant and $\tau_c = \sqrt{H_0/(g \cos \theta)}$, a characteristic time, with g the grav-
 541 itational acceleration. r_f and t_f are inversely proportional to the parameter $\Delta \tan =$
 542 $\tan \delta - \tan \theta$ and thus diverge when the slope angle θ tends towards δ . The scaling law
 543 for the runout distance r_f has been validated experimentally by *Farin et al.* [2014] for
 544 granular flows of various volumes and aspect ratios inside an inclined flume, below a crit-
 545 ical slope angle $\theta = 10^\circ - 16^\circ$. For slope angles θ above the critical angles the mea-
 546 sured runout distances r_f were observed to diverge from the scaling law because they
 547 begin to also depend on the initial column length D_0 .

548 In our experiments, the runout distance r_f and the flow duration t_f (or signal du-
 549 ration t_s , which is equal to t_f because of high signal-to-noise ratio) seem proportional
 550 to H_0 and τ_c , respectively, for a fixed slope angle θ (Fig. 12ab). In addition, r_f and t_s
 551 can be both well fitted by a law in $1/\Delta \tan$ for the whole investigated range of slope an-
 552 gles $\theta < 20^\circ$, in agreement with Eq. (10) and (11) (dashed lines in Fig. 12ab, see also
 553 Table 4). The critical slope angle above which the runout distance r_f does not fit the
 554 analytical scaling law (10) any more seems to be higher than $\theta = 20^\circ$. This is proba-
 555 bly because the friction angle of our steel particles ($\delta = 27^\circ$) is higher than the one in
 556 the experiments of *Farin et al.* [2014] ($\delta = 23^\circ$).



557 **Figure 12.** (a) Runout distance r_f as a function of the column initial height H_0 . (b) Signal
558 duration t_s as a function of characteristic time $\tau_c = \sqrt{H_0 / (g \cos \theta)}$. (c) to (e) Radiated seismic
559 energy W_{el} as a function of (c) initial height H_0 , (d) runout distance r_f and (e) signal duration
560 t_s , for different slope angles θ . In each panel, data for a given slope angle θ are fitted by a power
561 law $y = c(\theta)x^n$, with n an integer and the coefficient $c(\theta)$ is represented as a function of the slope
562 angle θ below each panel and fitted by a function of the parameter $\Delta \tan = \tan \delta - \tan \theta$ (dashed
563 line).

566 Interestingly, for a fixed slope angle θ , the seismic energy W_{el} correlates well with
 567 the column's initial height H_0 , the runout distance r_f and the flow/signal duration t_s
 568 as (Fig. 12cde)

$$569 \quad W_{el} = c_1(\theta)H_0^2, \quad (12)$$

$$570 \quad W_{el} = c_2(\theta)r_f^2, \quad (13)$$

$$571 \quad W_{el} = c_3(\theta)t_s^4. \quad (14)$$

572 These laws are consistent with each others because $r_f^2 \propto H_0^2$ and $t_s^4 \propto H_0^2$ (Eq. (10)
 573 and (11)). The relation $W_{el} \propto t_s^4$ was predicted analytically by *Hibert et al.* [2011] for
 574 granular flows on a flat slope. Coefficients $c_i(\theta)$ in the scaling laws can be well fitted with
 575 a function of the parameter $\Delta \tan$ (Fig. 12cde). A good fit for $c_1(\theta)$ ($R^2 = 0.99$) is (in
 576 kg s^{-2})

$$577 \quad c_1(\theta) \approx 2.15 \cdot 10^{-3} \left(\frac{0.081}{(\tan \delta - \tan \theta)^2} + 1 \right). \quad (15)$$

578 Using Eq. (12) and (15), we can very well fit the data of radiated seismic energy W_{el} as
 579 a function of θ for various mass M and aspect ratio a in Fig. 9ab, with no adjustments
 580 and using the real H_0 of each experiment and the friction angle $\delta = 27^\circ$ measured in-
 581 dependently for steel beads of diameter $d = 2$ mm. The proportionality coefficient in
 582 equation (15) equals $2.15 \cdot 10^{-3} \text{ kg s}^{-2}$ when $d = 2$ mm but depends on particle di-
 583 ameter as d^3 . Thus, for all of our experimental data (Fig. 11c),

$$584 \quad W_{el} \approx (5 \cdot 10^5 \text{ kg m}^{-3} \text{ s}^{-2}) \times d^3 H_0^2 \left(\frac{0.081}{(\tan \delta - \tan \theta)^2} + 1 \right). \quad (16)$$

585 A normalized law is given in Appendix C: . We can also express the radiated seismic en-
 586 ergy W_{el} as a function of r_f or t_f and the slope angle θ , by replacing H_0 in Eq. (16) us-
 587 ing Eq. (10) or (11), respectively.

588 From Eq. (8), (9) and (16), we finally deduce empirical expressions for the speeds
 589 $\max(V_{tot}^{COM})$ and $\max(V_{front})$ as a function of the other flow parameters (coefficients
 590 given in S.I. units, see Appendix C: for normalized laws)

$$591 \quad \max(V_{tot}^{COM}) \approx 36.5 \left(\frac{H_0^2}{M^{0.74}} \left(\frac{0.081}{(\tan \delta - \tan \theta)^2} + 1 \right) \right)^{\frac{1}{0.94}} \quad (17)$$

$$592 \quad \max(V_{front}) \approx 83.5 \left(\frac{H_0^2}{M^{0.73}} \left(\frac{0.081}{(\tan \delta - \tan \theta)^2} + 1 \right) \right)^{\frac{1}{1.04}} \quad (18)$$

593 Globally, our experimental data match well the scaling law for the maximum total bulk
 594 speed $\max(V_{tot}^{COM})$ ($R^2 = 0.76$) within an order of magnitude. However, the agreement

595 is less good for the maximum front speed $\max(V_{front})$ ($R^2 = 0.1$), probably because
 596 the position of the flow front is difficult to determine as the front is composed of saltat-
 597 ing particles, especially at high slope angles (Fig. 11de).

598 **4.2 Interpretation of the Empirical Scaling Laws with Particle Agita-** 599 **tion**

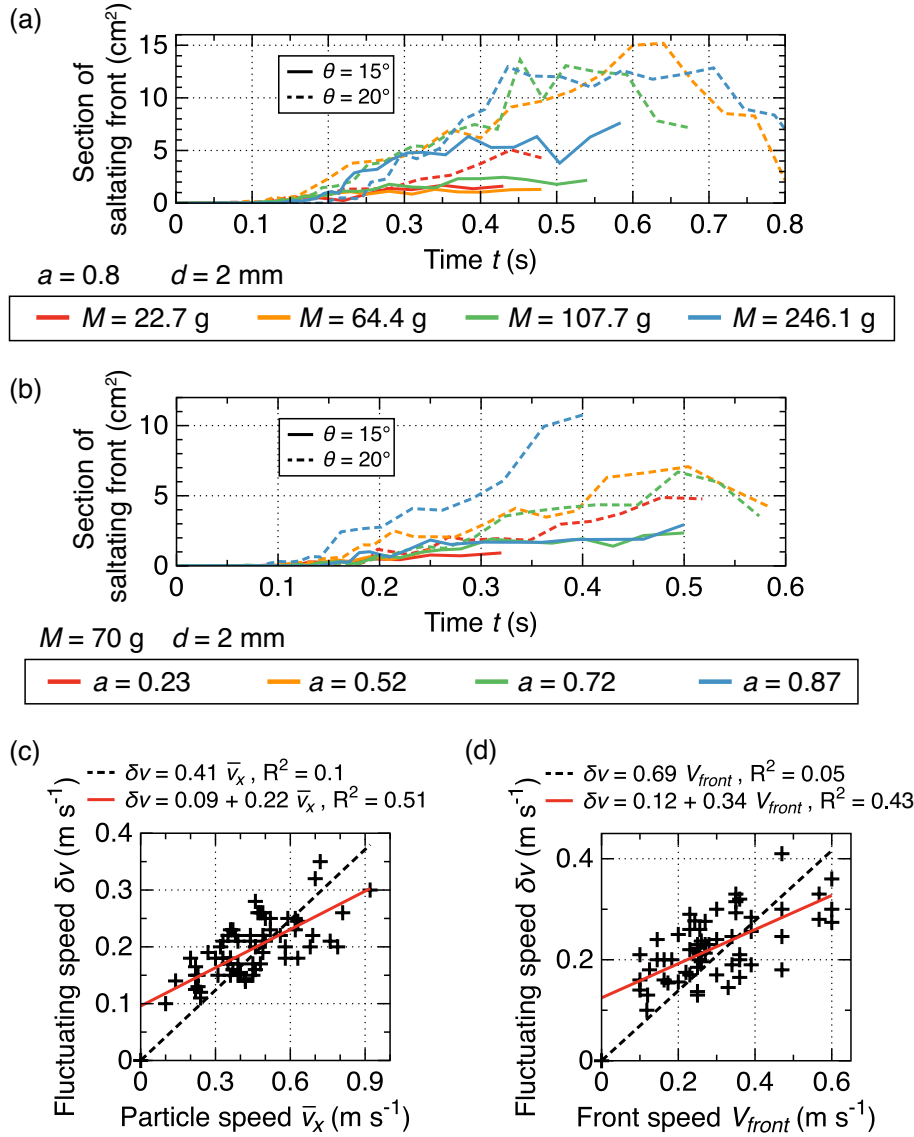
600 The amplitude of the seismic signal generated by granular flows is controlled by
 601 the rate of particle impacts R_{imp} at the bed and the impulse I_{imp} per particle impact
 602 on the bed. The rate of particle impact R_{imp} can be expressed as the number of impacts
 603 per particle per second per unit surface of the bed multiplied by the surface of the flow
 604 in contact with the bed. The impulse per particle I_{imp} is proportional to the mass of the
 605 particle multiplied by the particle impact speed. Individual particles in a granular flow
 606 have an average downslope speed and a fluctuating speed around their position [*Andreotti*
 607 *et al.*, 2013]. The fluctuating speed, that represents agitation of particles, is an impor-
 608 tant parameter that controls the rate at which particles impact each others and the bed
 609 but also controls the speed (i.e. the impulse) of the impacts on the bed. The fluctuat-
 610 ing speed is then a key dynamics parameter to measure to better understand the seis-
 611 mic emission by granular flows [*Bachelet et al.*, 2017, 2018b]. Any change of the granu-
 612 lar column initial dimensions or flow characteristics that increase the parameters R_{imp}
 613 and I_{imp} and the fluctuating speed thus also increase the radiated seismic energy W_{el} .
 614 The physical model for the seismic signal generated by debris flows proposed by *Farin*
 615 *et al.* [2019] shows that W_{el} scales in fact as $R_{imp}I_{imp}^2$ because the seismic amplitude gen-
 616 erated by the sum of the impacts at the bed in the debris flow increases as $I_{imp}\sqrt{N}$, with
 617 N the number of impacts.

618 In order to quantify particle agitation, we measured the surface of the region of saltat-
 619 ing particles in front of the flows (in the plane $(X, Y = 0, Z)$) (Fig. 13ab). Particle ag-
 620 itation is higher (i.e. the saltating surface is larger) as the slope angle θ , the flow mass
 621 M and the aspect ratio a increases. Saltation of particles at the flow front is quasi-absent
 622 at low slope angles $\theta < 10^\circ$ [*Farin et al.*, 2018], but increases significantly at high slope
 623 angles $\theta > 15^\circ$. Interestingly, we observe a linear correlation between the average fluctu-
 624 ating speed $\delta v = \sqrt{(v_X - \bar{v}_X)^2 + v_Z - \bar{v}_Z)^2}$ of flow particles, with v_i , the particle
 625 speed and \bar{v}_i , the average particle speed in i -direction (Fig. 13c). The best fit is $\delta v =$
 626 $0.09 + 0.22\bar{v}_X$. We also note a linear correlation between the fluctuating speed δv of par-

627 ticles at the flow front and the speed V_{front} of the flow front at the time of the measure-
628 ment (Fig. 13d). It is clear that a particle is more agitated when its speed or that of the
629 whole flow increases because the flow is more unstable. Note however, that we measured
630 the fluctuating speed of particles from the side of the flow and this speed may be lower
631 than that at the middle of the flow. More laboratory experiments or numerical simula-
632 tions are needed to link the radiated seismic energy W_{el} to the fluctuating speed δv of
633 particles at the bed of granular flows and understand how δv is controlled by the other
634 flow parameters (average flow speed in the case of steady granular flows, particle diam-
635 eter, slope angle, column mass, flow thickness and bed roughness).

644 In light of these observations, we can interpret the dependence of W_{el} to the col-
645 umn or flow characteristics by determining which characteristics increase the rate of im-
646 pacts R_{imp} , the impulse per impact I_{imp} and the particle fluctuating speed δv :

- 647 • When the flow speed or the slope angle θ increase, the rate of impacts per par-
648 ticle on the bed increases because particles are more agitated (δv increases) and
649 encounter bumps on the bed faster. Note that, similarly to particle agitation, the
650 radiated seismic energy W_{el} barely increases with slope angle θ for $\theta < 10^\circ$ but
651 diverges as the slope angle θ approaches the friction angle δ (Fig. 9ab and 13ab).
652 This confirms that the observed substantial increase of W_{el} at high slope angles
653 θ may be linked to a change of granular flow regime towards an agitated flow.
- 654 • When the column mass M , the slope angle θ , the runout distance r_f or the flow
655 duration t_s (which are both controlled by θ) increase, the surface of the flow in
656 contact with the bed increases, therefore the number of particle impacts at the
657 bed and W_{el} increase (Fig. 12de). The fact that W_{el} increases as r_f^2 is probably
658 because the surface of the deposit in contact with the bed increases as r_f^2 (with
659 the deposit width being proportional to the deposit length r_f).
- 660 • When the particle diameter d and the flow speed increase, particle impacts im-
661 part stronger impulses $I_{imp} \propto mv_{imp}$ on the bed. Indeed, the mass m of parti-
662 cles increases as d^3 and their impact speed v_{imp} increases as particle agitation δv
663 increases, which itself increases with flow speed (Figure 13cd). In addition, when
664 the initial column height H_0 or the aspect ratio a increase, the height of fall of the
665 particles increase and they also impact the bed stronger.



636 **Figure 13.** (a) and (b) Section of the saltating front as a function of time for $\theta = 15^\circ$ (full
637 lines) and $\theta = 20^\circ$ (dashed lines) and for (a) $a = 0.8$, $d = 2$ mm and different masses M (differ-
638 ent colors) and (b) $M = 70$ g, $d = 2$ mm and different column initial aspect ratios a (different
639 colors). (c) Fluctuating speed $\delta v = \sqrt{(v_x - \bar{v}_x)^2 + (v_z - \bar{v}_z)^2}$ of particles measured from video
640 recordings of various granular flows as a function of their average downslope speed \bar{v}_x (in the
641 X direction). (d) Fluctuating speed δv in the flow front as a function of the front speed V_{front} at
642 the same time. In panels (c) and (d), linear (thick red line) and scale (black dashed line) fits of
643 the data are shown with R^2 value.

666 4.3 Comparison with the Scaling Laws for a Single Particle Impact

667 *Farin et al.* [2015] demonstrated that for one single elastic impact of a particle on
 668 a smooth thin plate (without rough bed), the seismic energy radiated by the impact and
 669 the mean frequency of the generated seismic signal are related to the particle diameter
 670 d and normal impact speed v_Z as

$$671 \quad W_{el} \propto d^5 v_Z^{11/5}, \quad (19)$$

$$672 \quad f_{mean} \propto d^{-1} v_Z^{1/5}. \quad (20)$$

673 [*Bachelet et al.*, 2018a] verified that the scaling law for W_{el} is still valid when the particle
 674 impacts a rough bed made of particles glued on the thin plate. However, we observe
 675 in Fig. 7a that the empirical relation between the radiated seismic energy W_{el} and the
 676 particle diameter for a granular flow is different than that for a single particle impact
 677 because W_{el} clearly scales as d^3 and not as d^5 . For a granular flow, the relation between
 678 W_{el} and d can be explained as follows. The rate of particle impact per particle and per
 679 unit surface R_{imp} varies as d^{-3} (because there are less particles per unit surface as d in-
 680 creases) and the squared impulse per particle impact I_{imp}^2 increases as d^6 because the
 681 impulse is proportional to the particle mass $m \propto d^3$. Therefore, if we refer to the phys-
 682 ical model of *Farin et al.* [2019], then $W_{el} \propto R_{imp} I_{imp}^2 \propto d^3$, which is in agreement
 683 with our empirical observation.

684 For a granular flow, is not relevant to relate the radiated seismic energy W_{el} and
 685 the normal impact speed v_Z of the individual particles as we do for one single impact
 686 because each particle of the flow has a different speed at a given time. As discussed ear-
 687 lier, a more relevant particle speed to relate to W_{el} in granular flows is the fluctuating
 688 speed δv of the particles, in conjunction with the rate of particle impact (which has no
 689 meaning for a single impact).

690 We note that the mean frequency f_{mean} of the seismic signal generated by gran-
 691 ular flows decrease as as particle diameter d increases, in agreement with what is observed
 692 for a single impact (Fig. 7d). However, f_{mean} seems to depend less on d (at power -0.15)
 693 than for a single impact (power -1). The exact scaling law between f_{mean} and d is un-
 694 sure due to the large uncertainties on the frequency. The range of investigated particle
 695 diameters d may not be large enough to clearly determine the relation between f_{mean}
 696 and d . Moreover, the low dependence of f_{mean} on d in our experiments may be explained

697 by the fact that high frequencies are filtered out by the presence of the rough bed on the
698 plate, which was not present in the study of *Farin et al.* [2015].

699 **4.4 Comparison with the Field**

700 **4.4.1 Seismic efficiency**

701 Some field studies estimated the ratio of radiated seismic energy over the poten-
702 tial energy lost by the gravitational event $W_{el}/\Delta E_p$ (i.e. the seismic efficiency). From
703 site to site, $W_{el}/\Delta E_p$ varies over several orders of magnitude, from 10^{-6} to 0.25 [*Vila-*
704 *josana et al.*, 2008; *Deparis et al.*, 2008; *Hibert et al.*, 2011; *Lévy et al.*, 2015; *Farin et al.*,
705 2015; *Hibert et al.*, 2017c]. The discrepancy of $W_{el}/\Delta E_p$ observed in the field could po-
706 tentially be explained by a variation of the average, or characteristic, particle diameter
707 d or (less probably) a variation of the slope angle θ . Indeed, in our experiments, $W_{el}/\Delta E_p$
708 and W_{el}/E_k strongly increase with particle diameter as d^3 and also slightly depend on
709 the slope angle θ (Fig. 7bc and 9cdef). That said, the presence of a rough or erodible
710 bed on bedrock also strongly affects the seismic efficiency of granular flows in the field,
711 as discussed by *Bachelet et al.* [2018a] and *Farin et al.* [2018], but this effect is complex
712 and still not well understood. Moreover, contrary to laboratory experiments where im-
713 pacts are mostly elastic, impacts of natural rock blocks in the field are often plastic be-
714 cause the blocks can fracture themselves or the bed and break into pieces during impacts.
715 Consequently, energy ratios $W_{el}/\Delta E_p$ and W_{el}/E_k strongly depend on the mineralog-
716 ical composition of the impactors and the ground which can be very different from one
717 site to the other, thus causing further discrepancy. The energy budget of inelastic im-
718 pacts has been discussed in details by *Farin et al.* [2015].

719 **4.4.2 Relation between Radiated Seismic Energy and Flow Volume**

720 *Norris* [1994] and *Yamada et al.* [2012] observed that the maximum amplitude $A_{max} \propto$
721 $W_{el}^{0.5}$ of the seismic signal generated by large landslides ($V = 10^4 - 10^7 \text{ m}^3$) scales with
722 their volume V . In contrast, *Hibert et al.* [2011] reported a linear correlation between
723 the seismic energy radiated by rockfalls and their volume V ($V = 10 - 10^4 \text{ m}^3$). In
724 our experiments, the radiated seismic energy W_{el} scales as the flow mass M (which is
725 proportional to the flow volume V , for a given particle diameter d). Our results are then
726 in agreement with the observations of *Hibert et al.* [2011] but not with that of *Norris* [1994]

727 and *Yamada et al.* [2012], for which $W_{el} \propto M^2$. The discrepancy between the differ-
 728 ent studies may originate from different relative sizes of the events compared to the par-
 729 ticle size. Indeed, our experiments compare more with small rockfalls as those observed
 730 by *Hibert et al.* [2011] than to large landslides (which may also contains water) as that
 731 observed by *Norris* [1994] and *Yamada et al.* [2012]. Furthermore, the frequency range
 732 over which the radiated seismic energy W_{el} is measured may also affect the observed scal-
 733 ing law between W_{el} and M . Indeed, in the case of *Norris* [1994] and *Yamada et al.* [2012]
 734 studies, the distance between the source and the seismic stations is in general several tens
 735 of kilometers while the rockfalls recorded by *Hibert et al.* [2011] occur for 50 m to 2 km
 736 away from the seismic stations. Frequencies of the seismic signal are lower as the source/station
 737 distance increases. The scaling $W_{el} \propto M$ reported by *Hibert et al.* [2011] and in the present
 738 study may be more representative of high-frequency (> 1 Hz) processes that occur at
 739 the particle scale than the relation $W_{el} \propto M^2$ found by *Norris* [1994] and *Yamada et al.*
 740 [2012] that may be more representative of low-frequency (< 1 Hz), large scale processes
 741 (e.g. bulk motion). The state of damage of the ground over which the granular flow prop-
 742 agate and the presence of an erodible bed may also affect the relation between W_{el} and
 743 M , as it has been noted for single particle impacts [*Bachelet et al.*, 2018a]. The relation
 744 between W_{el} and M may also depend on the thickness of the impacted substrate. For
 745 example, *Farin et al.* [2015] demonstrated that the scaling laws between the mass and
 746 speed of an impacting particle and the characteristics of the generated seismic signal were
 747 different on a thin plate or thick block. We conducted some granular column collapse
 748 experiments on a thick marble block of dimensions $20 \times 20 \times 20$ cm³ (see Fig. A.1 in
 749 Appendix B:). On the thick block, the radiated seismic energy W_{el} increases as $M^{1.5}$
 750 and energy ratio $W_{el}/\Delta E_p$ is independent of M (Fig. A.1ab), in contrast to what is ob-
 751 served on the thin plate ($W_{el} \propto M^{1.0}$ and $W_{el}/\Delta E_p \propto M^{-0.3}$, Fig. 7ef). More ex-
 752 periments of granular flows on thick blocks are needed to better understand the effect
 753 of the thickness of the substrate on the empirical scaling laws and extrapolate them to
 754 the field.

755 **4.4.3 Relation between Radiated Seismic Energy and Flow Momentum**

756 For twelve large landslides that occurred worldwide between 1994 and 2014, *Hi-*
 757 *bert et al.* [2017a] reported that the amplitude of the seismic signal envelope filtered be-
 758 tween 3 and 10 Hz matches well temporally with the variation of the flow bulk momen-

759 tum in the downslope direction, inferred from the low-frequency content (< 0.1 Hz) of
760 the seismic signal. In addition, they found that the maximum envelope amplitude in-
761 creases linearly with the flow momentum MV_X^{COM} . Therefore, in their case $W_{el} \propto (M \max(V_X^{COM}))^2$.
762 In our experiments, the shape of the seismic envelope does not match with the speed of
763 the center of mass in X -direction and the maximum envelope amplitude matches bet-
764 ter with the maximum of the speed of the center of mass in the Z -direction (Fig. 5ag
765 and 10ac) [see also *Farin et al.*, 2018, for more details]. The best fit we observe is $W_{el} \propto$
766 $M^{0.74} \max(V_{tot}^{COM})^{0.94}$ (Fig. 10f), which is different by about a power of 2 from *Hibert*
767 *et al.* [2017a] scaling law.

768 The first explanation of this difference may be that the flows considered by *Hib-*
769 *ert et al.* [2017a] spend a longer proportion of their total duration with a motion in the
770 X -direction, with motion in the Z being almost null for most of the flow propagation.
771 Thus $V_{tot}^{COM} \approx V_X^{COM}$ in their case and the radiated seismic amplitude can only match
772 with flow motion in the X -direction. In contrast, in our experiments, flow motion in both
773 X and Z -directions contributes to the seismic generation and, in consequence, the ra-
774 diated seismic energy correlates well with the total speed of the center of mass (Fig. 11a).
775 The second explanation of the difference with the observations of *Hibert et al.* [2017a]
776 is the same as the one we invoked to explain why we observe $W_{el} \propto M$ instead of $W_{el} \propto$
777 M^2 as observed by *Norris* [1994] and *Yamada et al.* [2012]. In *Hibert et al.* [2017a] study,
778 the good correlation between the seismic envelope amplitude and the flow bulk momen-
779 tum in X -direction may more originate from bulk related processes (bulk motion, long-
780 scale topographic variations), while in our experiments seismic amplitude may more be
781 related to particle scale processes (particle diameter, speed fluctuations,...). Indeed, the
782 seismic signals of *Hibert et al.* [2017a] are recorded far from the flows and seismic sig-
783 nals are in a relatively low frequency range (3-10 Hz) while particle impacts in the field
784 can generate signals of frequency up to 150 Hz [e.g. *Helmstetter and Garambois*, 2010;
785 *Hibert et al.*, 2011; *Dammeier et al.*, 2011; *Farin et al.*, 2015; *Hibert et al.*, 2017c].

786 **4.4.4 Scaling Laws Between Flow Dynamic Parameters**

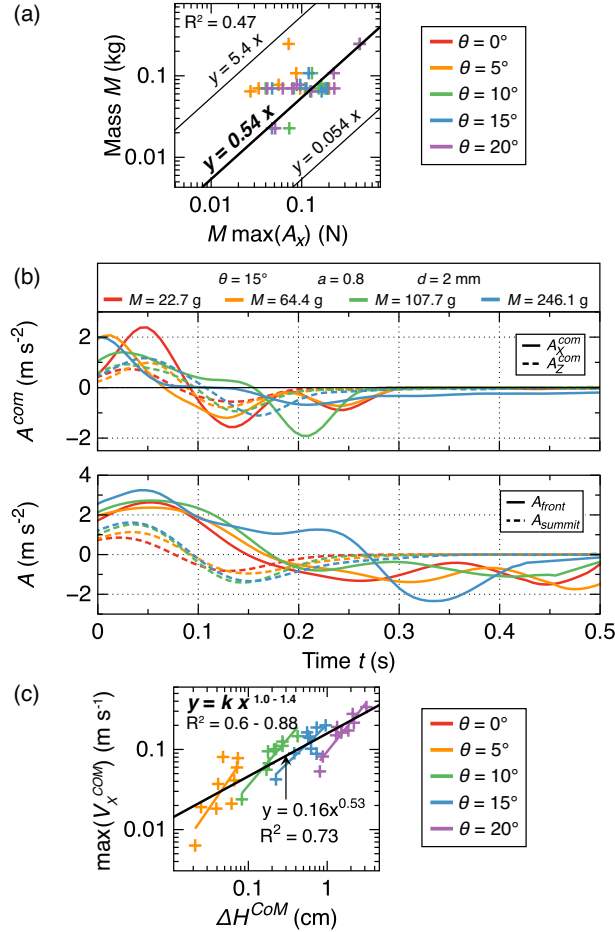
787 Aside from seismic waves generation by granular flows, we now discuss two empiri-
788 cal scaling laws reported in the literature between dynamic parameters of granular flows,
789 in light of our laboratory experiments.

790 *Ekström and Stark* [2013] reported the relation $M \approx (0.54 \text{ m}^{-1}\text{s}^2)F_{max}$ between
791 the mass M of 29 large landslides and the maximum force $F_{max} = M \max|A_X^{COM}|$ they
792 applied on the ground. The maximum force F_{max} is deduced by inversion of the low-frequency
793 seismic signals. Our experimental data also match this relation $M \approx 0.54M \max|A_X^{COM}|$,
794 within an order of magnitude (Fig. 14a). However, we observe that the peak bulk ac-
795 celeration $\max|A_X^{COM}|$ is approximately independent of the flow parameters and is about
796 $2 \pm 1 \text{ m s}^{-2}$ (Fig. 14b). Similarly, the peak bulk acceleration evaluated by *Ekström and*
797 *Stark* [2013] is about $2 \pm 1 \text{ m s}^{-2}$ for all landslides. As a consequence, the relationship
798 $M \approx 0.54M \max|A_X^{COM}|$ may be artificially caused by the fact that we are plotting the
799 mass M as a function of itself times a constant which is $(0.54 \text{ m}^{-1}\text{s}^2) \max|A_X^{COM}| \approx$
800 1.

808 For different large landslides that occurred in Japan and the ones reported by *Ek-*
809 *ström and Stark* [2013], *Yamada et al.* [2018] found a scaling law $\max(V_X^{COM}) \approx 2(\Delta H^{COM})^{0.5}$,
810 relating $\max(V_X^{COM})$, the maximum speed of the center of mass in the X -direction and
811 ΔH^{COM} , the height difference of the center of mass before and after the collapse. We
812 observe a similar scaling law in our experiments for $d = 2 \text{ mm}$ and different masses M
813 and aspect ratios a , with a power about 0.53 when we fit all of our data for all slope an-
814 gles θ (Fig. 14c). However, for a given slope angle θ , the maximum bulk speed seems to
815 increase as $\max(V_X^{COM}) \approx 2(\Delta H^{COM})^{1.2}$. Therefore, the relation reported by *Yamada*
816 *et al.* [2018] may be due to the fact that the different landslides occurred at different slope
817 angles θ . This illustrates an advantage of the laboratory experiments of granular flows
818 as the ones conducted in the present study: we can separate the different controlling pa-
819 rameters and better understand the link between different flow characteristics.

820 **4.5 What Flow Parameters Could Be Inverted from High-Frequency Seis-** 821 **mic Signals in the Field?**

822 The preceding sections showed that there are some differences between the scal-
823 ing laws reported in the field between dynamics and seismic characteristics of granular
824 flows and that observed in the laboratory. Even if an empirical scaling law represents
825 very well the laboratory data, for example $W_{el} \approx 1.3 \cdot 10^4 d^3 M^{0.74} \max(V_{tot}^{COM})^{0.94}$ (Fig.
826 11a), it is unclear that the exact same scaling law will match the field data because pro-
827 cesses are still not well understood, such as the effect of the complex bed topography on
828 the high-frequency seismic signal, how seismic energy is attenuated in a erodible bed or



801 **Figure 14.** (a) Mass M of the granular columns as a function of $M \max(A_X)$, with A_X , the
802 acceleration of the flow center-of-mass in the X -direction, for different slope angles (different
803 colors). (b) Acceleration of the center of mass in both X and Z -directions and acceleration of
804 the flow front and summit for $\theta = 15^\circ$, $a = 0.8$, $d = 2$ mm and different column's mass M . (c)
805 Maximum speed $\max(V_X^{COM})$ of the center of mass in the X -direction as a function of the height
806 difference ΔH^{COM} of the center of mass before and after the collapse, for different slope angles θ
807 (different colors).

829 particle segregation. Nevertheless, the empirical scaling laws established in the labora-
830 tory allow us to observe which flow properties have the strongest influence on a given
831 seismic characteristic and, therefore, may be inferred from this characteristic in the field.
832 Note that, however, if one wants to evaluate any flow properties quantitatively from the
833 seismic signal, we have to have a good estimate of the ground elastic parameters (den-
834 sity, quality factor and wave speeds), because these are necessary to compute the abso-
835 lute radiated seismic energy W_{el} [e.g. *Vilajosana et al.*, 2008; *Hibert et al.*, 2011; *Lévy*
836 *et al.*, 2015; *Hibert et al.*, 2017c]. Without these elastic parameters, we can only make
837 qualitative estimates of flow characteristics between successive granular flows [e.g. *Kean*
838 *et al.*, 2015].

839 **4.5.1 Particle diameter**

840 The radiated seismic energy W_{el} and the seismic efficiency ($W_{el}/\Delta E_p$ or W_{el}/E_k)
841 strongly depend on particle diameter as d^3 (Fig. 7abc). The characteristic particle di-
842 ameter d of the granular flow could thus be inverted from these parameters, provided
843 the other flow parameters also affecting these parameters (mass M , flow speed, aspect
844 ratio a) are known. The average frequency f_{mean} of the seismic signal generated by the
845 granular flows seem to only depend on the particle diameter d (Fig. 7d), then it could
846 be a useful parameter to obtain information on the characteristic particle diameter of
847 the granular flow. The relevant characteristic particle diameter contributing most to the
848 seismic signal amplitude depends on the particle size distribution. *Farin et al.* [2019] eval-
849 uated that this characteristic diameter corresponds to the 73th percentile of the parti-
850 cle size distribution (d_{73}) for a debris flow with a log-‘raised cosine’ particle size prob-
851 ability distribution. Note that if one would like to evaluate another flow parameter, the
852 characteristic particle diameter could also be determined from sampling of the deposits
853 of prior granular flows at the investigated site.

854 **4.5.2 Mass**

855 The only seismic parameters that seem to have a strong dependence on the flow
856 mass M is the radiated seismic energy W_{el} (Fig. 7e). Using relations as the ones in Eq.
857 (8) or (9), one could invert the flow mass M from W_{el} if the characteristic particle di-
858 ameter d and the flow speed are known.

859 **4.5.3 Aspect Ratio**

860 The radiated seismic energy W_{el} and the seismic to kinetic energy ratio W_{el}/E_k
861 clearly depend on the column initial aspect ratio a (Fig. 71k) and could thus potentially
862 give some quantitative information about this parameter if the particle diameter d can
863 be independently estimated.

864 **4.5.4 Flow Speed**

865 The average or frontal speed of the granular flows relate well with the radiated seis-
866 mic energy (Fig. 11ab). The flow speed could then be extrapolated from W_{el} if the char-
867 acteristic particle diameter d and the flow mass M are known. It is possible that, for nat-
868 ural granular flows, the correlation between the radiated seismic energy and the speed
869 of the flow front is better than in our experiments because large particle diameters of-
870 ten accumulate at the front of the flow due to particle segregation [Iverson, 1997].

871 If one wants to determine another flow parameter (flow mass M or particle diam-
872 eter d) from the radiated seismic energy W_{el} , the average flow speed could also be de-
873 termined from optical methods (cameras, laser distancemeters,...) or other seismic meth-
874 ods. For example, the trajectory of the flow center-of-mass and thus the average flow speed
875 could be deduced from low-frequency (< 0.1 Hz) signals for large landslides [Allstadt,
876 2013; Hibert *et al.*, 2014a]. Moreover, if two seismic stations are located a few meters away
877 along the flow path, the cross-correlation of the seismic signals measured could constrain
878 the time spent by the flow to travel from one station to the other and therefore the av-
879 erage flow speed between the two stations [Arattano and Marchi, 2005; Burtin *et al.*, 2010;
880 Kean *et al.*, 2015].

881 **4.5.5 Runout Distance and Flow Duration**

882 We observed a good correlation between the squared runout distance r_f^2 and the
883 radiated seismic energy W_{el} for a given slope angle θ (Fig. 12d). If the slope angle of a
884 specific site is known, one could potentially automatically evaluate the runout distance
885 of landslides occurring at a site from their radiated seismic energy. More work is how-
886 ever required to verify if the relation $W_{el} \propto r_f^2$ observed here for a constant flat slope
887 changes for a curved slope as one encounter in nature or for a different bed roughness.
888 Numerical simulations of granular flows coupled with a model of seismic generation by

889 impacts could also provide insights into the influence of complex bed topography on the
 890 relation between r_f and W_{el} . The duration of the flow approximates well with the du-
 891 ration of the seismic signal as long as the signal-to-noise ratio is high.

892 **4.5.6 Inversion Test**

893 We attempt to invert the particle diameter d , aspect ratio a and mass M of all of
 894 our released granular columns released from the characteristics of the generated seismic
 895 signal using the obtained empirical scaling laws. By inversion of the scaling laws in Ta-
 896 bles 2 and 3, we get (with coefficients in S.I. units, see Appendix C: for normalized laws)

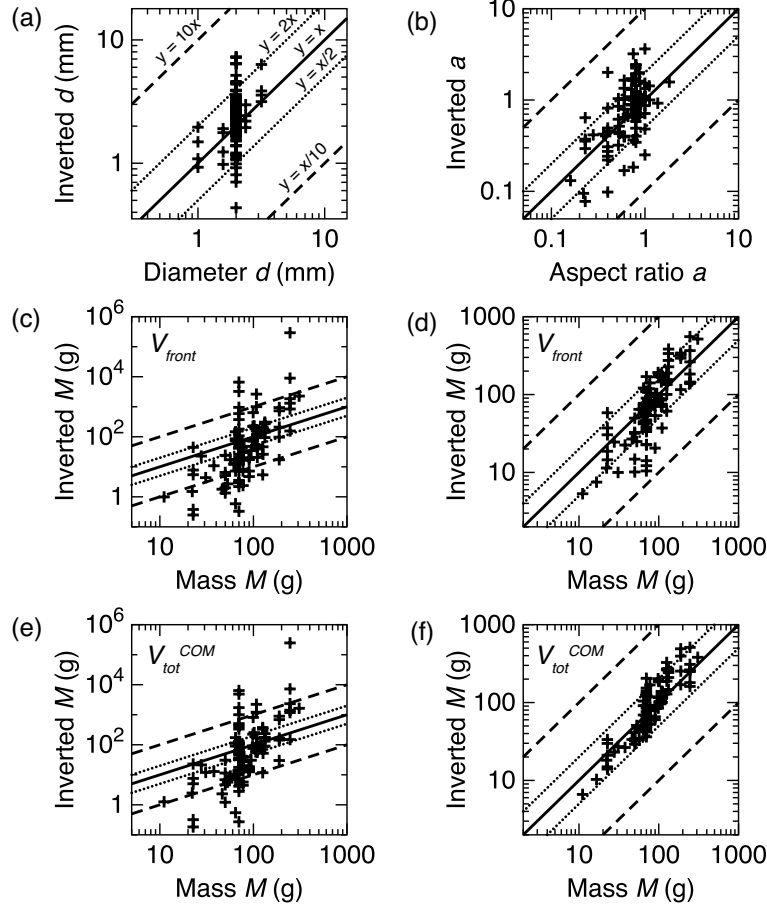
$$d \approx 2.77 \cdot 10^{22} (f_{mean})^{-6.66} \quad (21)$$

$$a \approx 0.014 \left(\frac{W_{el}}{E_k} \right)^{-0.77} \quad (22)$$

$$M \approx 6.67 \cdot 10^{-6} \left(\frac{W_{el}}{d^3 \max(V_{front})^{1.04}} \right)^{1.37} \quad (23)$$

$$M \approx 2.76 \cdot 10^{-6} \left(\frac{W_{el}}{d^3 \max(V_{tot}^{COM})^{0.94}} \right)^{1.35} . \quad (24)$$

897 Using these equations and if we assume that the flow speeds V_{front} and V_{tot}^{COM} (and
 898 thus kinetic energy E_k) can be measured e.g. using a camera or from low frequencies,
 899 one can retrieve d , a and M from a measurement of the mean frequency f_{mean} and the
 900 seismic energy W_{el} of the generated high-frequency seismic signal (Fig. 15). Most of the
 901 inverted particle diameters d and aspect ratios a using Eq. (21) and (22), respectively,
 902 are close to their real values, within a factor of two (Fig. 15ab). Using the diameters d
 903 inverted in Fig. 15a, one can also retrieve the flow mass M from the radiated seismic
 904 energy and the flow speeds using Eq. (23) and (24), but within more than an order of
 905 magnitude (Fig. 15ce). Estimating the particle diameter d from the signal frequency f_{mean}
 906 is somewhat imprecise because f_{mean} only has a small dependence to d at power -0.15
 907 (Table 2). If particle diameter is evaluated using another method described above, a much
 908 better estimation of the flow mass is obtained using the real particle diameters d , within
 909 a factor of 2 for most cases (Fig. 15df). A better agreement between inverted and real
 910 masses M is obtained using the speed of the center of mass V_{tot}^{COM} than when using the
 911 flow front speed V_{front} . Note that we doubt that the inverted scaling laws (21) to (24)
 912 could be directly applied to estimate the parameters of natural granular flows from the
 913 generated seismic signal because they are obtained in a simple, somewhat unrealistic,



916 **Figure 15.** Inversion of the parameters of all of the granular flows from seismic characteristics
 917 and the flow speeds using equations (21) to (24). (a) Particle diameter inverted from the mean
 918 frequency of the seismic signal f_{mean} . (b) Aspect ratio a inverted from the ratio W_{el}/E_k . (c) to
 919 (f) Mass M inverted from the radiated seismic energy W_{el} , diameter d with (c), (d) the speed of
 920 the flow front V_{front} , (e), (f) the total speed of the flow center of mass V_{tot}^{COM} and using (c), (e)
 921 the particle diameter inverted in (a) and (d), (f) the exact particle diameter d . Dashed lines are
 922 $y = 10x$ and $y = x/10$ laws, dotted lines are $y = 2x$ and $y = x/2$ laws and the full line is $y = x$.

914 configuration. However, they give insights into which seismic parameters have the strongest
 915 influence on a given flow characteristic.

923 5 Conclusions

924 We conducted laboratory experiments of 3D granular column collapse on an inclined
 925 flat thin plate. We successively varied the column mass and aspect ratio, the particle di-

926 ameter and the slope angle. The dynamic parameters of the granular flows were recorded
 927 using a fast camera and the generated seismic signal was measured using piezoelectric
 928 accelerometers. The conclusions of these experiments are as follows:

- 929 1. The observations of *Farin et al.* [2018] for one column mass, aspect ratio and par-
 930 ticle diameter remain valid when these parameters change. Specifically, the max-
 931 imum seismic amplitude coincides in time with the maximum flow speed in the
 932 direction normal to the bed. The seismic amplitude starts to depend on the flow
 933 motion in the downslope direction during the deceleration phase when flow mo-
 934 tion in normal direction has stopped. The shape of the temporal variation of the
 935 normalized radiated seismic energy and potential energy lost by the granular flow
 936 match and this shape changes when the slope angle is higher than a critical slope
 937 angle $\sim 15^\circ$.
- 938 2. Empirical scaling laws are established for the seismic characteristics as a function
 939 of the parameters of the granular column and of the deposit. The absolute radi-
 940 ated seismic energy scales with particle diameter as d^3 , column mass as M , as-
 941 pect ratio as $a^{1.1}$ and initial column height as H_0^2 when all other parameters are
 942 fixed. We also observe that the radiated seismic energy scales with the squared
 943 runout distance and with flow duration at power 4. The ratio of seismic energy
 944 over potential energy lost is between $3 \cdot 10^{-5}$ and $2 \cdot 10^{-3}$ and mostly increases
 945 with particle diameter as d^3 . The ratio of seismic energy over bulk kinetic energy
 946 is between $7 \cdot 10^{-4}$ and 10^{-1} increases as d^3 and decreases as $a^{-1.3}$. The average
 947 frequency of the radiated seismic signal only depends on the particle diameter as
 948 $d^{-0.15}$. The powers of these scaling laws do not strongly depend on slope angle.
- 949 3. Very good correlation is found for all of our experiments ($R^2 = 0.87 - 0.9$) be-
 950 tween the seismic energy radiated by the granular flows and two equivalent func-
 951 tions of the flow characteristics $d^3 M^{0.74} \max(V_{tot}^{COM})^{0.94}$ and $d^3 H_0^2 \left(\frac{0.081}{(\tan \delta - \tan \theta)^2} + 1 \right)$,
 952 with d , the particle diameter, M , the flow mass, V_{tot}^{COM} , the total speed of the flow
 953 center-of-mass, H_0 , the column initial height, δ , the friction angle and θ , the slope
 954 angle. The observed scaling laws allow us to determine which flow parameters could
 955 be inferred from a given seismic characteristic in the field. For example, particle
 956 diameter, flow mass or flow average speed can be deduced from the radiated seis-
 957 mic energy if the other two parameters can be determined independently. By as-
 958 suming the flow average speed is known, we show that we can retrieve parame-

959 ters d , a and M from the seismic signal within a factor of two. These scaling laws
960 provide insights into what relations can be tested in the field between flow and
961 seismic parameters.

962 4. We interpreted the scaling laws for the radiated seismic energy by discussing par-
963 ticle agitation in the flows. For example, the radiated seismic energy is almost con-
964 stant at small slope angle but significantly increases after a critical slope angle.
965 This increase correlates with a similar increase of particle agitation (fluctuating
966 speed) and, therefore, is probably caused by a change of the dynamic regime of
967 granular flows towards a more agitated flow. Moreover, the seismic efficiency de-
968 creases as slope angle increases but increases again at high slope angles, proba-
969 bly because the stronger particle agitation increases the radiated seismic energy
970 while not contributing much to bulk potential energy. More generally, any change
971 in the flow parameters that increases the particle fluctuating speed at the bed, which
972 controls the rate of particle impact and the force per impact on the bed, also in-
973 creases the radiated seismic energy. Fluctuating speed is therefore a crucial pa-
974 rameter to measure in future laboratory experiments in order to better understand
975 the link between flow parameters and the generated high-frequency (> 1 Hz) sei-
976 mic signal.

977 The present laboratory experiments provide an extensive set of data to test future
978 numerical simulations of the high-frequency seismic signal generated by granular flows.
979 Such simulations would be useful to better understand the quantitative link between the
980 fluctuating speed of particles (i.e. particle agitation) and the seismic energy radiated by
981 granular flows and the role of the complex bed topography on the shape of the seismic
982 signal. More seismically monitored experiments are also needed on an erodible bed be-
983 cause the structure of the flow/bed interface is thought to have a critical influence on
984 the high-frequency seismic efficiency of granular flows. Understanding these complex pro-
985 cesses (particle fluctuations in flows, effect of bed topography, erodible bed) is crucial
986 to be able to infer quantitative flow characteristics from seismic signals in the field in
987 the future, even if very clear empirical scaling laws can be established at the laboratory
988 scale.

989 **A: Granular Column Collapse Experiments on a Thick Block**

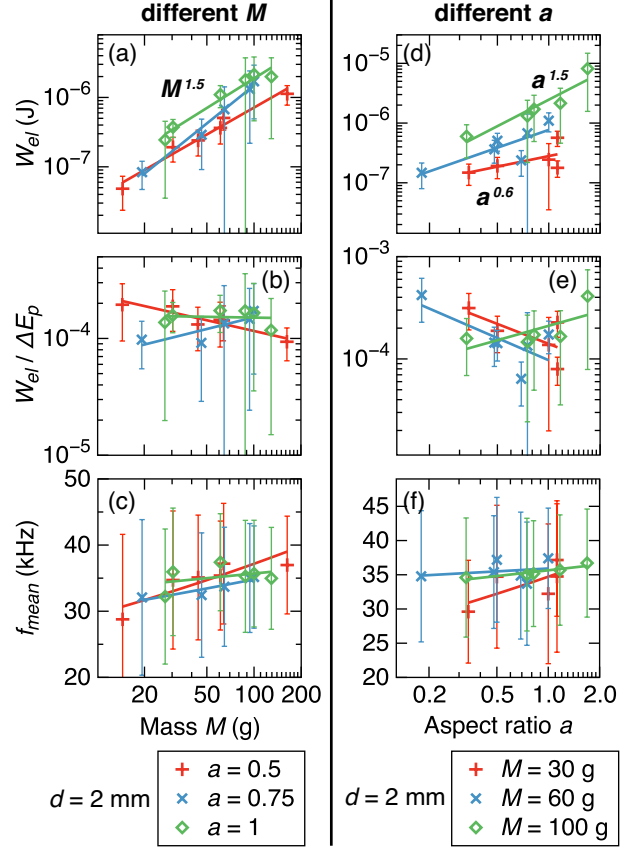
990 In order to verify how the scaling laws depend on the thickness of the substrate,
991 we conducted a series of granular column collapse experiments on a marble block of di-
992 mensions $20 \times 20 \times 20 \text{ cm}^3$ for various column masses $10 \text{ g} < M < 200 \text{ g}$ and aspect
993 ratios $0.2 < a < 2.0$. The radiated seismic energy W_{el} , the ratio of W_{el} over the po-
994 tential energy lost ΔE_p and the mean frequency f_{mean} measured in these experiments
995 are shown in Fig. A.1. Similar scaling laws to the thin plate case are observed for the
996 aspect ratio a (Fig. A.1def). The mean frequency f_{mean} seems to very slightly increase
997 with M and a (Fig. A.1cf). Refer to section 4.4.2 for discussion of the data as a func-
998 tion of the column's mass M .

1005 **B: Seismic Signals and Comparison with Dynamics for Different As-** 1006 **pect Ratios**

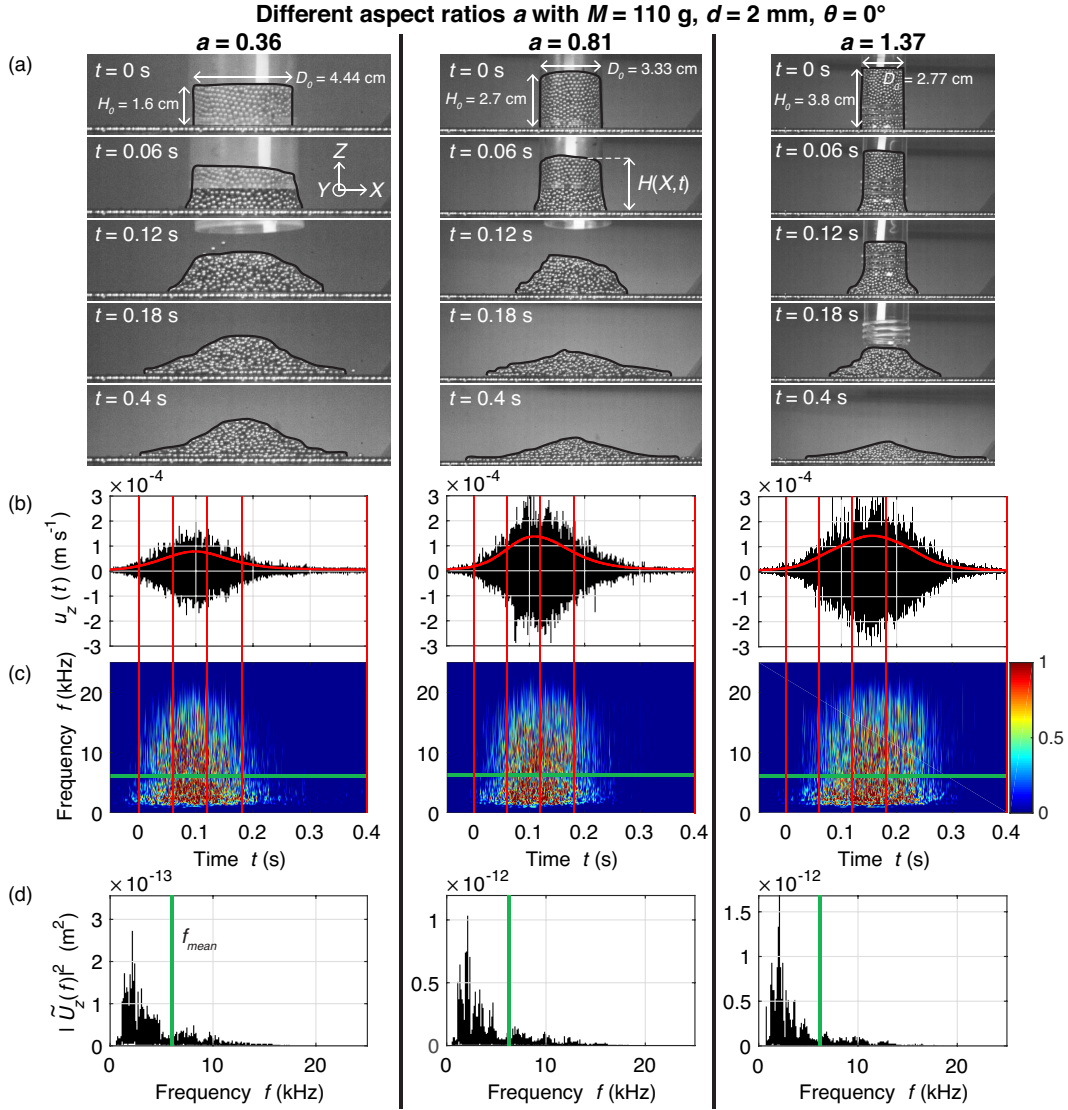
1007 In this Appendix, we show seismic signals and spectrograms for different aspect ra-
1008 tios and fixed mass $M = 110 \text{ g}$ and particle diameter $d = 2 \text{ mm}$, for slope angles $\theta =$
1009 0° and $\theta = 15^\circ$ (Fig. B.1 and B.2). The comparison of the seismic signals with the dy-
1010 namic characteristics of the granular flows for different aspect ratios at $\theta = 0^\circ$ and $\theta =$
1011 15° and for different masses at $\theta = 0^\circ$ is shown in Fig. B.3, B.4 and B.5. Refer to sec-
1012 tion 3 for discussion of these Figures.

1036 **C: Normalized Scaling Laws**

1037 In this section, we give a normalization of the scaling laws obtained in the manuscript.
1038 We normalize the parameters by those for one single impact of a steel particle of diam-
1039 eter $d_{part} = 1 \text{ mm}$, mass $M_{part} = 4 \cdot 10^{-6} \text{ kg}$, impact speed $V_{part} = \sqrt{gd} \approx 0.1 \text{ m s}^{-1}$
1040 and fall height $H_{part} = d/2$. Therefore, the normalized parameters are $d' = d/d_{part}$,
1041 $M' = M/M_{part}$, $\max(V_{tot}^{COM})' = \max(V_{tot}^{COM})/V_{part}$, $\max(V_{front})' = \max(V_{front})/V_{part}$
1042 and $H'_0 = H_0/H_{part}$. The radiated seismic energy W_{el} is normalized by the theoret-
1043 ical radiated seismic energy for the impact of a steel particle with the above character-
1044 istics on the PMMA plate, $W_{part} \approx 8.85 \cdot 10^{-11} \text{ J}$ [Farin et al., 2015]. The kinetic en-
1045 ergy is normalized by the kinetic energy of the impact $E_{part} = \frac{1}{2}M_{part}V_{part}^2 \simeq 2 \cdot 10^{-8} \text{ J}$.
1046 Then, the normalized energies are $W'_{el} = W_{el}/W_{part}$ and $E'_k = E_k/E_{part}$. The fre-
1047 quency is normalized by 1 Hz.



999 **Figure A.1.** Seismic parameters as a function of the granular column parameters for the ex-
1000 periments on a marble block of dimensions $20 \times 20 \times 20 \text{ cm}^3$. (a),(d) Radiated seismic energy
1001 W_{el} , (b),(e) Ratio of W_{el} over the potential energy lost ΔE_p , (c),(f) Mean frequency f_{mean} of the
1002 seismic signal for (a) to (c) different masses M for $d = 2 \text{ mm}$ and fixed aspect ratios a and (d)
1003 to (f) different aspect ratios a for $d = 2 \text{ mm}$ and fixed masses M . Data are fitted by power laws
1004 (full lines). The power law is indicated when a tendency is observed.



1013 **Figure B.1.** (a) Successive pictures of three horizontal ($\theta = 0^\circ$) granular column collapse
1014 experiments with different aspect ratios $a = 0.36$, $a = 0.81$ and $a = 1.37$, all with initial column
1015 mass $M = 110$ g and particle diameter $d = 2$ mm. The black lines show the contours $H(X, t)$
1016 of the granular flows that are used to compute the flow dynamic parameters. (b) Seismic signals
1017 (i.e. plate vibration speed $u_z(t)$) generated by the granular flows as a function of time t . The
1018 red line represent the amplitude envelope, filtered below 5 Hz. (c) Spectrograms of the signals.
1019 Warmer colors mean more energy (normalized to 1). (d) Squared amplitude spectra $|\tilde{U}_z(f)|^2$ of
1020 the seismic signals. The vertical red lines in panels (b) and (c) indicate the times of the pictures
1021 in (a) and the thick green line in panels (c) and (d) indicates the mean frequency f_{mean} of the
1022 signals.

Different aspect ratios a with $M = 70$ g, $d = 2$ mm, $\theta = 15^\circ$

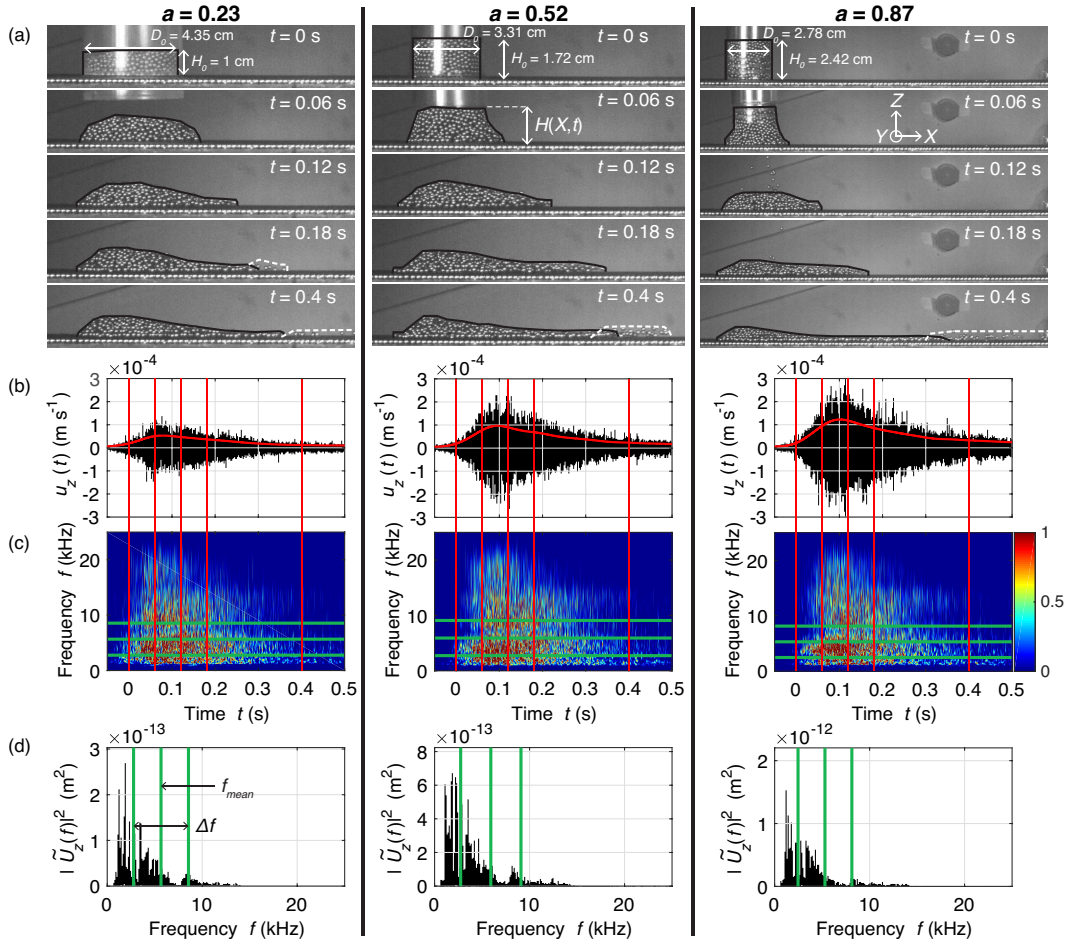
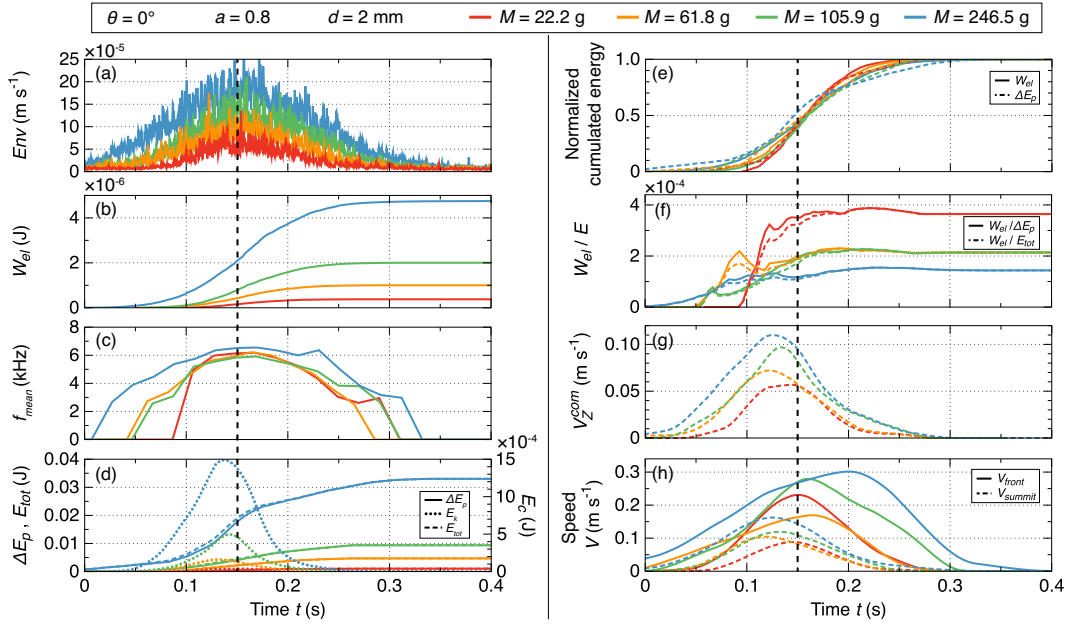
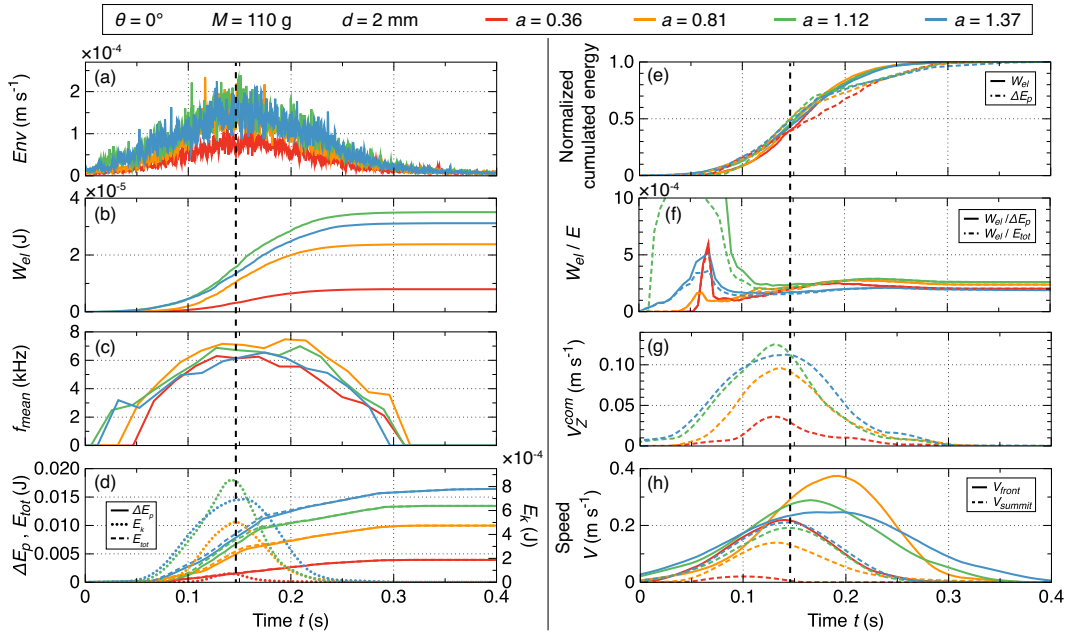


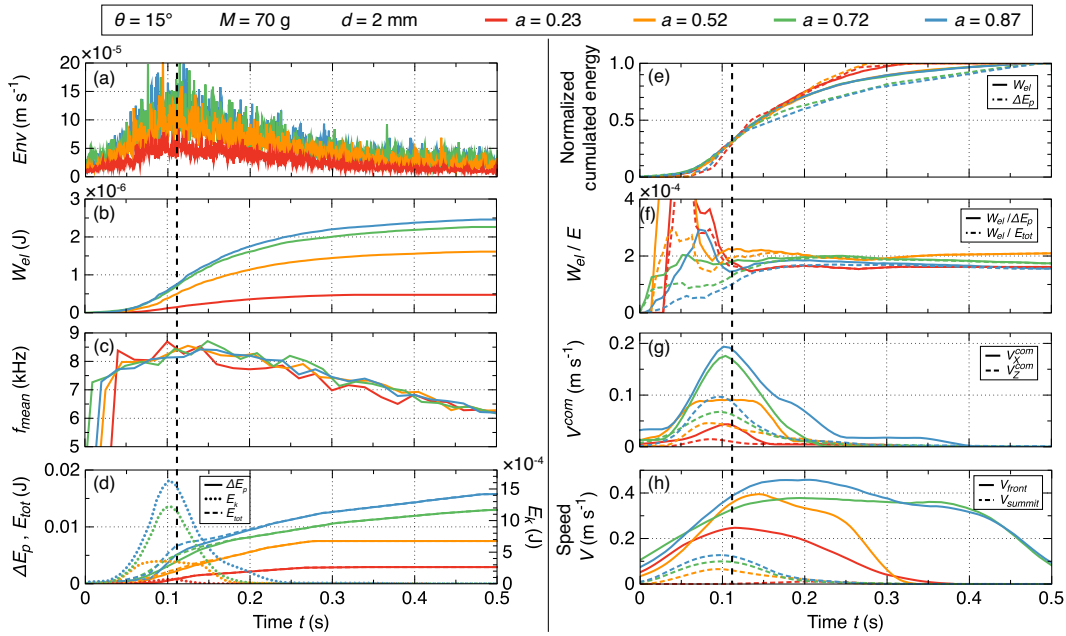
Figure B.2. Same as in Fig. B.1 but for slope angle $\theta = 15^\circ$.



1024 **Figure B.3.** Comparison of the dynamics of granular flows with the generated seismic signal
 1025 for $\theta = 0^\circ$, $a = 0.8$, $d = 2$ mm and different column masses M (different colors). (a) Enve-
 1026 lope $Env(t)$ of the seismic signal filtered below 100 Hz. (b) Radiated seismic energy $W_{el}(t)$.
 1027 (c) Mean frequency f_{mean} . (d) Potential energy lost ΔE_p , kinetic energy E_k and total energy
 1028 $E_{tot} = \Delta E_p + E_k$. (e) Normalized cumulated radiated seismic energy $W_{el}(t)$ and potential energy
 1029 lost ΔE_p . (f) Ratio of the radiated seismic energy over the potential energy lost and the total
 1030 energy lost. (g) Speed V_Z^{COM} of the flow center-of-mass in the Z -direction. (h) Speed V_{front} and
 1031 V_{summit} of the flow front (in X -direction) and of the flow summit (in Z -direction).



1032 **Figure B.4.** Same as Fig. B.3 but for $\theta = 0^\circ$, $M = 110$ g, $d = 2$ mm and different column ini-
 1033 tial aspect ratios a (different colors).



1034 **Figure B.5.** Same as Fig. B.3 but for $\theta = 15^\circ$, $M = 70$ g, $d = 2$ mm and different column ini-
 1035 tial aspect ratios a (different colors).

Table C.1. Normalized scaling laws.

$$\begin{aligned}
W'_{el} &\approx 160E_k'^{0.5} \\
&\approx 88.2E_k'^{0.56} \\
&\approx 1.7d'^3M'^{0.74}\max(V_{tot}^{COM})'^{0.94} \\
&\approx 0.7d'^3M'^{0.73}\max(V_{front})'^{1.04} \\
\hline
W'_{el}/H_0'^2 &\approx 0.48/(\tan\delta - \tan\theta)^2 + 6.07 \\
\hline
W'_{el} &\approx 1.4d'^3H_0'^2\left(\frac{0.081}{(\tan\delta - \tan\theta)^2} + 1\right) \\
\hline
\max(V_{tot}^{COM})' &\approx 0.6\left(\frac{H_0'^2}{M'^{0.74}}\left(\frac{0.081}{(\tan\delta - \tan\theta)^2} + 1\right)\right)^{\frac{1}{0.94}} \\
\max(V_{front})' &\approx 2.3\left(\frac{H_0'^2}{M'^{0.73}}\left(\frac{0.081}{(\tan\delta - \tan\theta)^2} + 1\right)\right)^{\frac{1}{1.04}} \\
\hline
d' &\approx 2.77 \cdot 10^{25} (f'_{mean})^{-6.66} \\
a' &\approx 0.014 \left(\frac{W'_{el}}{E'_k}\right)^{-0.77} \\
M' &\approx 1.6 \left(\frac{W'_{el}}{d'^3 \max(V_{front})'^{1.04}}\right)^{1.37} \\
M' &\approx 0.48 \left(\frac{W'_{el}}{d'^3 \max(V_{tot}^{COM})'^{0.94}}\right)^{1.35}.
\end{aligned}$$

1049

Notation

1050

 A_{max} Maximum amplitude of the seismic signal (m s⁻¹)

1051

 a Aspect ratio $a = H_0/D_0$ (-)

1052

 D_0, H_0 Initial diameter and thickness of the granular column (m)

1053

 d Bead diameter (m)

1054

 $\Delta E_p, E_p, E_k, E_{tot}$ Potential energy lost, potential energy, bulk kinetic energy and total energy lost (J)

1055

1056

 $Env(t)$ Amplitude envelope of the seismic signal (m s⁻¹)

1057

 f, ω Frequency and angular frequency (s⁻¹)

1058

 f_{mean} Mean frequency of the signal (Hz)

1059

 g Gravitational acceleration (m s⁻²)

1060

 $H(X, t), l(Z, t)$ Thickness and length profiles of the flow contour in the $(X, Y = 0, Z)$ plane (m)

1061

1062

 h, V_p Thickness (m) and volume (m³) of the plate

1063

 I_{imp} Impulse per particle impact (N s)

1064

 M Mass of the granular flow (kg)

1065

 m Mass of a particle (kg)

1066

 R_{imp} Rate of particle impact (s⁻¹)

1067

 r_f Runout distance (m)

1068

 t Time (s)

1069

 t_s, t_f Duration of the seismic signal and duration of the flow motion (s)

1070

 u_z, a_z Normal vibration speed (m s⁻¹) and acceleration (m s⁻²) of the plate surface

1071

 \tilde{U}_Z Time Fourier transform of u_z (m s⁻¹/Hz)

1072

 V Flow volume (m³)

1073

 V_i^{COM}, V_{tot}^{COM} Speed of the center of mass in the i direction and total speed (m s⁻¹)

1074

 V_{front}, V_{summit} Speeds of the flow front and summit (m s⁻¹)

1075

 u_z Impact speed of individual particles in the Z -direction (m s⁻¹)

1076

 v_z Impact speed (m s⁻¹)

1077

 W Width of the granular flow in the Y -direction (m)

1078

 W_{el} Seismic energy radiated during the impact (J)

1079

 X, Y, Z Coordinates in the reference frame of the inclined plate (m)

1080

 X^{COM}, Z^{COM} Coordinates of the flow center of mass in the X and Z -directions (m)

1081 X^{front}, Z^{summit} Coordinates of the flow front and flow maximum height in the X
1082 and Z -directions (m)
1083 δ Friction angle ($^{\circ}$)
1084 θ Slope angle ($^{\circ}$)
1085 ρ_p Density of the plate (kg m^3)
1086 τ, γ Characteristic time (s) and coefficient (1/m) of energy attenuation
1087 τ_c Characteristic duration of a granular flow (s)

1088 Acknowledgments

1089 This work was supported by the Agence Nationale de la Recherche ANR LANDQUAKES,
1090 REALISE, ITN FLOWTRANS and ERC Contract No. ERC-CG-2013-PE10-617472 SLID-
1091 EQUAKES. The data used in this paper can be found at the following address: .

1092 References

- 1093 Aki, K., and P. Richards (1980), *Quantitative Seismology : Theory and Methods*,
1094 vol. 1, W.H. Freeman.
- 1095 Allstadt, K. (2013), Extracting source characteristics and dynamics of the August
1096 2010 Mount Meager landslide from broadband seismograms, *J. Geophys. Res.*,
1097 *118*(3), 1472–1490, doi:10.1002/jgrf.20110.
- 1098 Andreotti, B., Y. Forterre, and O. Pouliquen (2013), *Granular Media: Between Fluid*
1099 *and Solid, vol. 1*, Cambridge Univ. Press.
- 1100 Arattano, M. (2000), On Debris Flow Front Evolution Along a Torrent, *Phys. Chem.*
1101 *Earth (B)*, *25*(9), 733–740, doi:10.1016/S1464-1909(00)00094-0.
- 1102 Arattano, M., and F. Moia (1999), Monitoring the propagation of a debris flow along
1103 a torrent, *Hydrol. Sci. J.*, *44*, 811–823, doi:10.1080/02626669909492275.
- 1104 Arattano, M., and L. Marchi (2005), Measurements of debris flow velocity through
1105 cross-correlation of instrumentation data, *Natural Hazards and Earth System*
1106 *Sciences*, *5*, 137–142.
- 1107 Bachelet, V., A. Mangeney, R. Toussaint, and J. de Rosny (2017), Seismic signal of
1108 near steady uniform flows, *AGU Fall Meeting*.
- 1109 Bachelet, V., A. Mangeney, J. De Rosny, R. Toussaint, and M. Farin (2018a), Elastic
1110 wave generated by granular impact on rough and erodible surfaces, *J. Applied*

1111 *Phys.*, 123, 044,901, doi:10.1063/1.5012979.

1112 Bachelet, V., A. Mangeney, R. Toussaint, and J. de Rosny (2018b), Which dynamic
1113 properties can be recovered from the seismic signal of steady and uniform granular
1114 flows ?, *EGU General Assembly*.

1115 Balmforth, N. J., and R. R. Kerswell (2005), Granular collapse in two dimensions, *J.*
1116 *Fluid Mech.*, 538(1), 399–428, doi:10.1017/S0022112005005537.

1117 Barrière, J., A. Krein, A. Oth, and R. Schenkluhn (2015), An advanced signal pro-
1118 cessing technique for deriving grain size information of bedload transport from
1119 impact plate vibration measurements, *Earth Surf. Process. Landforms*, 40, 913–
1120 924, doi:10.1002/esp.3693.

1121 Brodsky, E., E. Gordeev, and H. Kanamori (2003), Landslide basal fric-
1122 tion as measured by seismic waves, *Geophys. Res. Lett.*, 30(24), 2236, doi:
1123 10.1029/2003GL018485.

1124 Burtin, A., L. Bollinger, R. Cattin, J. Vergne, and J. L. Nábělek (2009), Spatiotem-
1125 poral sequence of Himalayan debris flow from analysis of high-frequency seismic
1126 noise, *J. Geophys. Res.*, 114(F4), F04,009.

1127 Burtin, A., J. Vergne, L. Rivera, and P. Dubernet (2010), Location of river-induced
1128 seismic signal from noise correlation functions, *Geophys. J. Int.*, 182(3), 1161–
1129 1173.

1130 Dammeier, F., J. R. Moore, F. Haslinger, and S. Loew (2011), Characterization of
1131 alpine rockslides using statistical analysis of seismic signals, *J. Geophys. Res.*,
1132 116(F4), F04,024, doi:10.1029/2011JF002037.

1133 Delannay, R., A. Valance, A. Mangeney, O. Roche, and P. Richard (2017), Gran-
1134 ular and particle-laden flows: from laboratory experiments to field observa-
1135 tions, *Journal of Physics D: Applied Physics*, 50(5), 053,001, doi:10.1088/1361-
1136 6463/50/5/053001.

1137 Deparis, J., D. Jongmans, F. Cotton, L. Baillet, F. Thouvenot, and D. Hantz (2008),
1138 Analysis of rock-fall and rock-fall avalanche seismograms in the French Alps, *Bull.*
1139 *Seism. Soc. Am.*, 98(4), 1781–1796, doi:10.1785/0120070082.

1140 Ekström, G., and C. P. Stark (2013), Simple Scaling of Catastrophic Landslide Dy-
1141 namics, *Science*, 339(6126), 1416–1419.

1142 Farin, M., A. Mangeney, and O. Roche (2014), Fundamental changes of gran-
1143 ular flow dynamics, deposition, and erosion processes at high slope angles:

1144 Insights from laboratory experiments, *J. Geophys. Res.*, *119*, 504–532, doi:
1145 10.1002/2013JF002750.

1146 Farin, M., A. Mangeney, R. Toussaint, J. de Rosny, N. Shapiro, T. Dewez, C. Hi-
1147 bert, C. Mathon, O. Sedan, and F. Berger (2015), Characterization of rockfalls
1148 from seismic signal: Insights from laboratory experiments, *J. Geophys. Res.*, *120*,
1149 doi:10.1002/2015JB012331.

1150 Farin, M., A. Mangeney, J. de Rosny, R. Toussaint, J. Sainte-Marie, and N. Shapiro
1151 (2016), Experimental validation of theoretical methods to estimate the energy
1152 radiated by elastic waves during an impact, *J. Sound Vib.*, *362*, 176–202, doi:
1153 10.1016/j.jsv.2015.10.003.

1154 Farin, M., A. Mangeney, J. de Rosny, R. Toussaint, and T. Phuong-Thu (2018),
1155 Link Between the Dynamics of Granular Flows and the Generated Seismic Signal:
1156 Insights From Laboratory Experiments, *J. Geophys. Res.: Earth Surface*, *123*,
1157 doi:10.1029/2017JF004296.

1158 Farin, M., V. Tsai, M. Lamb, and K. Allstadt (2019), A physical model for the
1159 high-frequency seismic signal generated by debris flows, *Earth Surf. Process. Land-*
1160 *forms*, doi:10.1002/esp.4677.

1161 Favreau, P., A. Mangeney, A. Lucas, G. Crosta, and F. Bouchut (2010), Nu-
1162 merical modeling of landquakes, *Geophys. Res. Lett.*, *37*, L15,305, doi:
1163 10.1029/2010GL043512.

1164 GdR Midi (2004), On dense granular flows, *Eur. Phys. J. E*, *14*(4), 341–365, doi:
1165 10.1140/epje/i2003-10153-0.

1166 Helmstetter, A., and S. Garambois (2010), Seismic monitoring of Séchilienne rock-
1167 slide (French Alps): Analysis of seismic signals and their correlation with rainfalls,
1168 *J. Geophys. Res.*, *115*, F03,016, doi:10.1029/2009JF001532.

1169 Hibert, C., A. Mangeney, G. Grandjean, and N. M. Shapiro (2011), Slope instabili-
1170 ties in Dolomieu crater, Réunion Island: From seismic signals to rockfall charac-
1171 teristics, *J. Geophys. Res.*, *116*, F04,032, doi:10.1029/2011JF002038.

1172 Hibert, C., G. Ekström, and C. Stark (2014a), Dynamics of the Bingham Canyon
1173 Mine landslides from seismic signal analysis, *Geophys. Res. Lett.*, *41*, 4535–4541,
1174 doi:10.1002/2014GL060592.

1175 Hibert, C., A. Mangeney, G. Grandjean, C. Baillard, D. Rivet, N. M. Shapiro, C. Sa-
1176 triano, A. Maggi, P. Boissier, V. Ferrazzini, and W. Crawford (2014b), Automated

1177 identification, location, and volume estimation of rockfalls at piton de la fournaise
1178 volcano, *J. Geophys. Res.*, *119*(5), 1082–1105, doi:10.1002/2013JF002970.

1179 Hibert, C., G. Ekström, and C. P. Stark (2017a), The relationship between bulk-
1180 mass momentum and short-period seismic radiation in catastrophic landslides, *J.*
1181 *Geophys. Res.*, *122*, 1201–1215, doi:10.1002/2016JF004027.

1182 Hibert, C., A. Mangeney, G. Grandjean, A. Peltier, A. DiMuro, N. Shapiro, V. Fer-
1183 razzini, P. Boissier, V. Durand, and P. Kowalski (2017b), Spatio-temporal evolu-
1184 tion of rockfall activity from 2007 to 2011 at the Piton de la Fournaise volcano
1185 inferred from seismic data, *J. Volcano. Geotherm. Res.*, *333–334*, 36–52, doi:
1186 10.1016/j.jvolgeores.2017.01.007.

1187 Hibert, C., J. Malet, F. Bourrier, F. Provost, F. Berger, P. Bornemann, P. Tardiff,
1188 and E. Mermin (2017c), Single-block rockfall dynamics inferred from seismic sig-
1189 nal analysis, *Earth Surf. Dynam.*, *5*, 283–292, doi:10.5194/esurf-5-283-2017.

1190 Hogg, A. J. (2007), Two-dimensional granular slumps down slopes, *Phys. Fluids*, *19*,
1191 093,301, doi:10.1063/1.2762254.

1192 Hsu, L., W. E. Dietrich, and L. S. Sklar (2014), Mean and fluctuating basal forces
1193 generated by granular flows: Laboratory observations in a large vertically rotating
1194 drum, *J. Geophys. Res.*, *119*(6), 1283–1309, doi:10.1002/2013JF003078.

1195 Huang, C.-J., C.-L. Shieh, and H.-Y. Yin (2004), Laboratory study of the un-
1196 derground sound generated by debris flows, *J. Geophys. Res.*, *109*(F1), doi:
1197 10.1029/2003JF000048.

1198 Huang, C.-J., H.-Y. Yin, C.-Y. Chen, C.-H. Yeh, and C.-L. Wang (2007), Ground
1199 vibrations produced by rock motions and debris flows, *J. Geophys. Res.*,
1200 *112*(F02014), doi:10.1029/2005JF000437.

1201 Iverson, R. (1997), The physics of debris flows, *Reviews of Geophysics*, *35*, 245–296,
1202 doi:10.1029/97RG00426.

1203 Kean, J., J. Coe, V. Coviello, J. Smith, S. McCoy, and M. Arattano (2015), Estimat-
1204 ing rates of debris flow entrainment from ground vibrations, *J. Geophys. Res.*, *42*,
1205 doi:10.1002/2015GL064811.

1206 Lai, V., V. Tsai, M. Lamb, T. Ulizio, and A. Beer (2018), The Seismic Signature
1207 of Debris Flows: Flow Mechanics and Early Warning at Montecito, California,
1208 *Geophys. Res. Lett.*, *45*, 5528–5535, doi:10.1029/2018GL077683.

1209 Lévy, C., A. Mangeney, F. Bonilla, C. Hibert, E. Calder, P. Smith, and P. Cole
1210 (2015), Friction weakening in granular flows deduced from seismic records at
1211 the Souffrière Hills Volcano, Montserrat, *J. Geophys. Res.*, *120*, 7536–7557, doi:
1212 10.1002/2015JB012151.

1213 Lube, G., H. E. Huppert, R. S. J. Sparks, and A. Freundt (2005), Collapses
1214 of two-dimensional granular columns, *Phys. Rev. E*, *72*(4), 041,301, doi:
1215 10.1103/PhysRevE.72.041301.

1216 Lube, G., H. E. Huppert, R. S. J. Sparks, and A. Freundt (2011), Granular col-
1217 umn collapses down rough, inclined channels, *J. Fluid Mech.*, *675*, 347–368, doi:
1218 10.1017/jfm.2011.21.

1219 Mangeney, A., O. Roche, O. Hungr, N. Mangold, G. Faccanoni, and A. Lucas
1220 (2010), Erosion and mobility in granular collapse over sloping beds, *J. Geophys.*
1221 *Res.*, *115*(F3), F03,040, doi:10.1029/2009JF001462.

1222 Moretti, L., A. Mangeney, Y. Capdeville, E. Stutzmann, C. Huggel, D. Schnei-
1223 der, and F. Bouchut (2012), Numerical modeling of the Mount Steller landslide
1224 flow history and of the generated long period seismic waves, *Geophys. Res. Lett.*,
1225 *39*(16), doi:10.1029/2012GL052511.

1226 Moretti, L., K. Allstadt, A. Mangeney, Y. Capdeville, E. Stutzmann, and
1227 F. Bouchut (2015), Numerical modeling of the Mount Meager landslide con-
1228 strained by its force history derived from seismic data, *J. Geophys. Res.*, *120*,
1229 2579–2599, doi:10.1002/2014JB011426.

1230 Norris, R. D. (1994), Seismicity of rockfalls and avalanches at three cascade range
1231 volcanoes: Implications for seismic detection of hazardous mass movements, *Bull.*
1232 *Seism. Soc. Am.*, *84*(6), 1925–1939.

1233 Pérez-Guillén, C., B. Sovilla, E. Suriñach, M. Tapiac, and A. Köhler (2016), De-
1234 ducing avalanche size and flow regimes from seismic measurements, *Cold Regions*
1235 *Science and Technology*, *121*, 25 – 41, doi:10.1016/j.coldregions.2015.10.004.

1236 Royer, D., and E. Dieulesaint (2000), *Elastic Waves in Solids I: Free and Guided*
1237 *Propagation*, Springer.

1238 Schneider, D., P. Bartelt, J. Caplan-Auerbach, M. Christen, C. Huggel, and B. W.
1239 McArdell (2010), Insights into rock-ice avalanche dynamics by combined analysis
1240 of seismic recordings and a numerical avalanche model, *J. Geophys. Res.*, *115*(F4),
1241 F04,026, doi:10.1029/2010JF001734.

1242 Siavoshi, S., and A. Kudrolli (2005), Failure of a granular step, *Phys. Rev. E*, *71*(5),
1243 051,302, doi:10.1103/PhysRevE.71.051302.

1244 Suriñach, E., I. Vilajosana, G. Khazaradze, B. Biescas, G. Furdada, and J. M. Vila-
1245 plana (2005), Seismic detection and characterization of landslides and other mass
1246 movements, *Nat. Hazards Earth Syst. Sci.*, *5*(6), 791–798, doi:10.5194/nhess-5-
1247 791-2005.

1248 Taylor, S., and E. Brodsky (2017), Granular temperature measured experimentally
1249 in a shear flow by acoustic energy, *Phys. Rev. E.*, *96*, 032,913.

1250 Turkaya, S., R. Toussaint, F. Eriksen, M. Zecevic, G. Daniel, E. Flekky, and
1251 K. J. Mly (2015), Bridging aero-fracture evolution with the characteristics of
1252 the acoustic emissions in a porous medium, *Frontiers in Physics*, *3*, 70, doi:
1253 10.3389/fphy.2015.00070.

1254 Turquet, A., R. Toussaint, F. Eriksen, G. Daniel, D. Koehn, and E. Flekky (2018),
1255 Microseismic emissions during pneumatic fracturing: A numerical model to ex-
1256 plain the experiments, *Journal of Geophysical Research: Solid Earth*, *123*(8),
1257 6922–6939, doi:10.1029/2017JB014613.

1258 Turquet, A., R. Toussaint, F. Eriksen, G. Daniel, O. Lenglin, E. Flekky, and K. Mly
1259 (2019), Source localization of microseismic emissions during pneumatic fracturing,
1260 *Geophysical Research Letters*, *46*(7), 3726–3733, doi:10.1029/2019GL082198.

1261 Vilajosana, I., E. Suriñach, A. Abellan, G. Khazaradze, D. Garcia, and J. Llosa
1262 (2008), Rockfall induced seismic signals: case study in Montserrat, Catalonia, *Nat.*
1263 *Hazards Earth Syst. Sci.*, *8*(4), 805–812, doi:10.5194/nhess-8-805-2008.

1264 Yamada, M., Y. Matsushi, M. Chigira, and J. Mori (2012), Seismic recordings of
1265 landslides caused by Typhoon Talas (2011), Japan, *Geophys. Res. Lett.*, *39*(13),
1266 doi:10.1029/2012GL052174.

1267 Yamada, M., A. Mangeney, Y. Matsushi, and L. Moretti (2016), Estimation
1268 of dynamic friction process of the Akatani landslide based on the waveform
1269 inversion and numerical simulation, *Geophys. J. Int.*, *206*, 1479–1486, doi:
1270 10.1093/gji/ggw216.

1271 Yamada, M., A. Mangeney, Y. Matsushi, and T. Matsuzawa (2018), Estimation
1272 of dynamics friction and movement history of large landslides, *Landslides*, doi:
1273 10.1007/s10346-018-1002-4.

1274 Yohannes, B., L. Hsu, W. Dietrich, and K. Hill (2012), Boundary stresses due to
1275 impacts from dry granular flows, *J. Geophys. Res.*, *117*, F02,027.

1276 Zhao, J., L. Moretti, A. Mangeney, E. Stutzmann, H. Kanamori, Y. Capdeville,
1277 E. Calder, C. Hibert, P. Smith, P. Cole, and A. LeFriant (2015), Model space ex-
1278 ploration for determining landslide source history from long-period seismic data,
1279 *Pure Appl. Geophys.*, *172*(2), 389–413, doi:10.1007/s00024-014-0852-5.